Journal of Computational Physics 450 (2022) 110823

Contents lists available at ScienceDirect

Journal of Computational Physics

www.elsevier.com/locate/jcp

Nonlinear mixed-dimension model for embedded tubular networks with application to root water uptake

Timo Koch [a,b,*], Hanchuan Wu [b], Martin Schneider [b]

[a] Department of Mathematics, University of Oslo, Postboks 1053 Blindern, 0316 Oslo, Norway
[b] Department of Hydromechanics and Modelling of Hydrosystems, University of Stuttgart, Pfaffenwaldring 61, 70569 Stuttgart, Germany

ARTICLE INFO

Article history:
Available online 10 November 2021

Keywords:
Mixed-dimension method
Embedded networks
1d-3d Coupling
Root water uptake
Smoothing kernel
Nonlinear elliptic equations

ABSTRACT

We present a numerical scheme for the solution of nonlinear mixed-dimensional PDEs describing coupled processes in embedded tubular network system in exchange with a bulk domain. Such problems arise in various biological and technical applications such as in the modeling of root-water uptake, heat exchangers, or geothermal wells. The nonlinearity appears in form of solution-dependent parameters such as pressure-dependent permeability or temperature-dependent thermal conductivity. We derive and analyze a numerical scheme based on distributing the bulk-network coupling source term by a smoothing kernel with local support. By the use of local analytical solutions, interface unknowns and fluxes at the bulk-network interface can be accurately reconstructed from coarsely resolved numerical solutions in the bulk domain. Numerical examples give confidence in the robustness of the method and show the results in comparison to previously published methods. The new method outperforms these existing methods in accuracy and efficiency. In a root water uptake scenario, we accurately estimate the transpiration rate using only a few thousand 3D mesh cells and a structured cube grid whereas other state-of-the-art numerical schemes require millions of cells and local grid refinement to reach comparable accuracy.

1. Introduction

Nonlinear elliptic equations arise in the description of fluid flow in porous media where permeability depends on the water pressure (e.g. Richards' equation) or the description of heat conduction where the thermal conductivity depends on temperature. In this work, we discuss a numerical scheme to solve such equations in the presence of an embedded thin tubular transport system exchanging mass or energy with the embedding bulk domain. This exchange is modeled by local source terms and results in coupled systems of mixed-dimensional partial differential equations. A motivating example is the simulation of root water uptake from soil when considering complex three-dimensional root network architectures explicitly [1], which allows to predict the complex water distribution in the soil around roots.

Consider a bounded Lipschitz domain $\Omega \subset \mathbb{R}^3$ with an embedded tubular network. The tube centerlines form a network of curves connected at branching points which is denoted by Λ, as shown in Fig. 1. In this work, we want to discuss stationary mixed-dimensional nonlinear equation systems of the form

* Corresponding author at: Department of Mathematics, University of Oslo, Postboks 1053 Blindern, 0316 Oslo, Norway.
E-mail address: timokoch@math.uio.no (T. Koch).

https://doi.org/10.1016/j.jcp.2021.110823

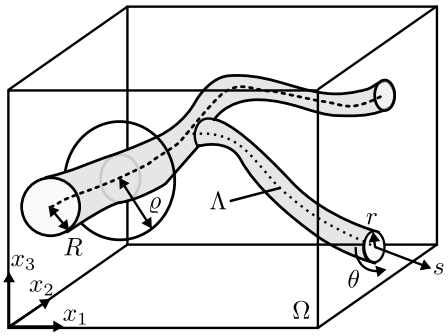

Fig. 1. Embedded tubular network system. The network of line segments Λ with radius function R is embedded into the bulk domain Ω. The subdomains Ω and Λ are equipped with the (local) coordinate systems (x_1, x_2, x_3) and (r, θ, s), respectively. Source terms coupling equations on Λ and Ω are distributed in the neighborhood of Λ in Ω, i.e. $r \leq \varrho(s)$. This technique allows to bridge the dimensional gap between the one-dimensional equations describing processes in Λ and the three-dimensional equations describing processes in Ω.

$$-\nabla \cdot \left(D_b(\hat{u}_b)\nabla \hat{u}_b\right) = q\delta_\Lambda \qquad \text{in} \quad \Omega, \tag{1.1a}$$

$$-\partial_s \left(D_e \partial_s u_e\right) = -q \qquad \text{on} \quad \Lambda, \tag{1.1b}$$

$$q := -|P|\gamma \left(\Pi_P \hat{u}_b - u_e\right), \tag{1.1c}$$

with suitable boundary conditions on $\partial\Omega$ and $\partial\Lambda$. In the specific case of network branches ending in Ω, we always impose no-flow (Neumann) boundary conditions. We assume $M : [0, 1] \to \mathbb{R}^3$, $s \mapsto \boldsymbol{x}$ to be a parametrization of Λ. The operators $\nabla\cdot$ and ∇ are the spatial divergence and gradient operators in Ω, and ∂_s denotes the derivative in direction of s. The scalar unknowns in Ω and Λ are denoted by $\hat{u}_b$ (b for "bulk") and u_e (e for "embedded"). The diffusion coefficients $D_b > 0$ and $D_e > 0$ are positive and continuous and D_b is a (possibly nonlinear) function of u_b. In the source term, γ is a diffusive permeability and $P = P(s)$ is the cross-sectional tube perimeter at s. Moreover, Π_P is an average operator such that $\Pi_P \hat{u}_b$ denotes the average of $\hat{u}_b$ on the perimeter P for a given s,

$$\Pi_P u := \frac{1}{|P|} \int_P u \, \mathrm{d}\zeta, \tag{1.2}$$

where ζ is some suitable parameterization of P in $\mathbb{R}^3$. Furthermore, we introduce

$$\hat{u}_b^{\bigcirc}(s) := \Pi_P \hat{u}_b(s), \tag{1.3}$$

explicitly referring to the average of $\hat{u}_b$. The term δ_Λ in Eq. (1.1a) restricts the source term on the centerline in the sense of distributions. That means, we define the right-hand-side of Eq. (1.1a) as a line source

$$q\delta_\Lambda := \int_0^1 \delta(M(s) - \boldsymbol{x}) q(s) \mathrm{d}s \tag{1.4}$$

where δ is the Dirac delta distribution. From definition (1.4) follows the property

$$\int_\Omega q\delta_\Lambda \eta(\boldsymbol{x}) \mathrm{d}\boldsymbol{x} = \int_\Lambda q(s)\eta(M(s)) \mathrm{d}s, \quad \forall \eta \in C^\infty(\Omega), \tag{1.5}$$

that is for all smooth test functions η, provided that q has sufficient regularity. For a discussion of the regularity requirements, we refer to [2–4]. We remark that the given formulation of the property includes the simpler case $\eta = 1$ in Ω. Property (1.5) implies that the balanced quantity (e.g. mass) is conserved.

The mixed-dimensional model (1.1) based on line sources, can be derived from a corresponding model with the three-dimensional tubular network structure cut out from Ω, by assuming that the tube radii R are much smaller than average distance between tubes [5,4]. We remark that the well-posedness of problem (1.1) for constant D_b has been shown in weighted Sobolev spaces in [2].

The water distribution around a three-dimensional root network taking up water from the embedding soil can be modeled by Eq. (1.1a) [6–8,1]. In this case, the unknowns are hydraulic pressures in root and soil, and D_b corresponds to the hydraulic conductivity. Soil can be viewed as a three-phasic porous medium composed of the solid matrix and two fluid phases, air and water. With decreasing water content the soil's hydraulic conductivity decreases drastically, and at the same time, capillary forces increase which attract water to the hydrophilic solid matrix [9]. Under the assumptions of local mechanical equilibrium a direct and nonlinear relationship between the local water pressure and the hydraulic conductivity

can be found [10,11]. At low water saturation, high pressure gradients are necessary to move water in dry soil. According to the cohesion-tension theory [12,13], transpiration at the plant leaves causes a high suction potential in plant roots and plants can maintain water uptake even in relatively dry soils. The root water uptake rate (q) is proportional to the root-soil pressure difference [7]. This can cause large local pressure gradients around roots [13,14] which are difficult to approximate with standard numerical schemes. We will use root water uptake as the motivational application and in the numerical examples in this work.

Problem (1.1) also arises for heat conduction problems, for example when modeling the temperature distribution around geothermal well systems [15,16]. Here, D_b corresponds to the thermal conductivity, which generally depends on temperature [17]. When modeling the flow field around a well in a confined aquifer under high injection rates the surrounding rock undergoes deformations. The hydraulic conductivity of the rock depends on the pore pressure.

The paper is structured as follows. Motivated by the results of [18], in Section 2 we propose a distributed source model to replace problem (1.1). In Section 3, we design a numerical scheme to accurately approximate the interface unknowns and hence Eq. (1.1c), locally for each tubular segment. The resulting reconstruction algorithm in the presence of nonlinear coefficient D_b—and the extensions of the ideas of [18] to that case—is the main contribution of this work. The method is based on local analytical solution obtained by means of Kirchhoff transformation. In Section 4, we show and discuss numerical results. In particular, in Sections 4.3.1 and 4.3.2 we investigate the reconstruction scheme numerically for a series of carefully constructed verification scenarios. Finally, in Section 4.4, we simulate root water uptake with a realistic root network obtained from MRI measurement and compare our results against a numerical reference solution obtained with state-of-the-art methods.

2. The distributed source model

The introduced model formulation (1.1), leads to solutions $\hat{u}_b$ which exhibit singularities on Λ. It is therefore difficult to construct efficient and accurate numerical schemes for solving problem (1.1) [3,4,18]. However, for a precise description of the source term coupling the network and bulk domain, it is crucial to accurately approximate the solution in the neighborhood of the network. Koch et al. [18] suggest to solve a modified problem

$$-\nabla\cdot(D_b(u_b)\nabla u_b) = q\Phi_\Lambda \qquad \text{in} \quad \Omega, \tag{2.1a}$$

$$-\partial_s(D_e\partial_s u_e) = -q \qquad \text{on} \quad \Lambda, \tag{2.1b}$$

$$q = -|P|\gamma(\hat{u}_b^{\bigcirc} - u_e), \tag{2.1c}$$

with the same boundary conditions as for problem (1.1), and where Φ_Λ denotes a set of non-negative kernel functions $\Phi_{\Lambda,i}$ that distribute q around a vessel segment i over a small radially-symmetric tubular support region with radius $\varrho(s) > 0$ and $\Phi_{\Lambda,i} = 0$ outside the support region (compact support), cf. Fig. 1. We point out that problem (2.1) has a modified solution denoted by u_b that is usually close to $\hat{u}_b$ but may differ significantly in the neighborhood of the network. Moreover, the source term (2.1c) depends on $\hat{u}_b^{\bigcirc}$ rather than $u_b^{\bigcirc}$, an important distinction that will become clear in the following, in particular in Section 3, where we explain how to compute $\hat{u}_b^{\bigcirc}$ for problem (2.1).

Remark 1. We choose kernel functions $\Phi_{\Lambda,i}(s)$ along each segment i in the form [18]

$$\Phi_{\Lambda,i}(\varrho) = \varrho^{-2}\varphi(r\varrho^{-1}) \quad \text{with} \quad \int_0^{2\pi}\int_0^{\varrho(s)} \Phi_{\Lambda,i} r \,\mathrm{d}r\mathrm{d}\theta = 1 \quad \forall s, \tag{2.2}$$

where the function φ is a positive symmetric mollifier [19,20] defined on a disc perpendicular to the vessel segment, cf. Fig. 1. An example for such kernel functions is given in Eq. (2.3). The kernel functions Φ_Λ have dimension L^{-2} (L: length) and bridge the dimensional gap of 2 between Eq. (2.1a) and Eq. (2.1b). In this work we use a uniform distribution,

$$\Phi_{\Lambda,i}(r) = \begin{cases} \frac{1}{\pi\varrho^2} & r \le \varrho, \\ 0 & r > \varrho. \end{cases} \tag{2.3}$$

Remark 2. For $\varrho \to 0$, such kernel functions $\Phi_{\Lambda,i}$ converge to Dirac delta functions in the sense of distributions [21]. In this sense, problem (2.1) is close to problem (1.1). However, solutions to (2.1) with $\varrho > 0$ have higher regularity than solutions to (1.1). Moreover, we emphasize that the limiting case $\varrho \to 0$ is not interesting in practice, and it is known that solutions to problem (1.1) are difficult to approximate numerically [3]. Instead, both problems (2.1) and (1.1) shall be considered approximations of the more accurate resolved interface model, where the bulk-network interface is explicitly resolved and the mass exchange is formulated in terms of boundary conditions on that interface, cf. [22,23]. In Section 4, we will show that solving problem (2.1) with $\varrho > R$ can yield better approximations to the solution of the fully-resolved model problem on coarse computational grids than solving problem (1.1).

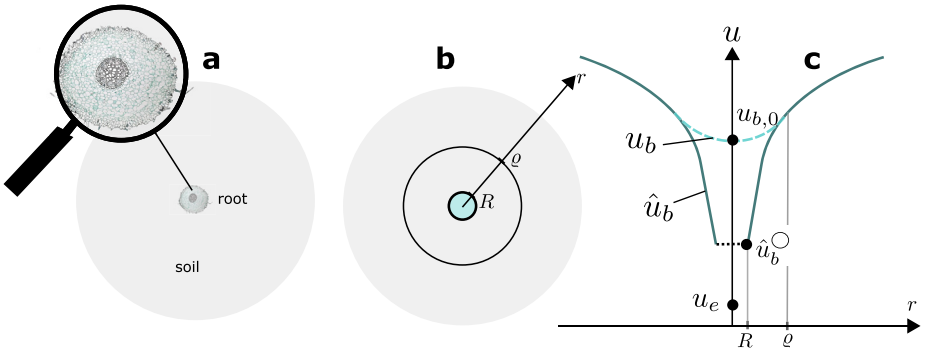

Fig. 2. The distributed source model. (A) Exemplary application: root water uptake from soil. Cross-sectional cut through root embedded in soil. (B) Terminology for radial symmetric setup, root radius and kernel support radius for local source distribution. (C) Effect of the regularization kernel on the local soil pressure solution. Symbols: $u_{b,0}$, regularized unknown at the tube centerline; $\hat{u}_b^{\bigcirc}$, (average) bulk interface quantity (e.g. soil pressure); u_e, physical quantity inside the tube (e.g. root pressure); R, tube radius; ϱ, kernel support radius.

Remark 3. For $\varrho \leq R$, $\hat{u}_b^{\bigcirc}$ can be approximated by $\Pi_P u_b$. However, for $\varrho > R$, this approximation is poor as the distribution kernel leads to a locally regularized solution $u_b \neq \hat{u}_b$ (visualized in Fig. 2). Hence, an algorithm approximating $\hat{u}_b$ from u_b in the latter case is required and will be presented in Section 3.

When simulating systems with large networks of thousands of tubes (e.g. root systems) resolving the local solution around each network segment requires fine local computational meshes. The kernel distributes the source or sink term in a local neighborhood around network segments. This leads to a smooth u_b which is easy to approximate by standard numerical schemes, see Fig. 2 for schematic representation at the example of a root segment cross-section. Unfortunately, the value of u_b at the tube-bulk interface does not correspond to the interface value of the line source model (1.1) anymore, i.e. $\Pi_P u_b \neq \hat{u}_b^{\bigcirc}$. In the following, we exploit the fact that we know *how* the introduced kernel function modifies the local solution around a single isolated tube segment. The design of a method to reconstruct $\hat{u}_b^{\bigcirc}$ accurately from the smooth solution u_b- in the presence of the nonlinearity introduced by the diffusion coefficient D_b- is discussed subsequently in Section 3 and is the main contribution of this work.

Finally, we recall that the linear case, that is $D_b = \text{const.}$, is discussed in [18]. For the particular case of root water uptake, local corrections based on the analytical solutions of the Richards equation have been proposed in [24]. However, the scheme is only presented in the discrete setting for a single voxel. The authors of [14] suggest to solve local radial-symmetric problems at every root segment, introducing additional unknowns. Again, the method is only presented in the discrete setting. In this work, we follow [18] and present a model formulated in a continuous setting which allows generalization to any suitable discretization method and simplifies the analysis of possible sources of errors. Moreover, the source distribution kernel allows to control the accuracy of the interface reconstruction in interplay with the mesh size. Apart from getting rid of singularities, problem formulation (2.1) has the advantage that it does not require that the computational grid resolves the length scale R to yield accurate approximations of q [3], but relaxes this requirement to the grid being required to resolve the length scale ϱ, a selectable model parameter. It has been demonstrated [18] that this formulation allows to significantly reduce the error in q, u_e, and u_b for coarse grids.

3. Local reconstruction of interface unknown and flux

In this section, we describe a method to accurately reconstruct the interface unknown $\hat{u}_b^{\bigcirc}$ for a given tube segment from the evaluation of the smoothed solution u_b on the centerline Λ. The Kirchhoff transformation, well-known from the solution of heat conduction problems [25, Eq. (10)] allows us to transform Eq. (2.1a) such that the nonlinearity only appears in the source term. We then derive a local analytical solution for u_b depending on tube and kernel radius. From this analytical solution, we deduct a nonlinear equation to compute $\hat{u}_b^{\bigcirc}$ from a point evaluation of u_b. We conclude by discussing the validity of the approach for the case of tubular networks.

3.1. Kirchhoff transformation

Equation (2.1) is a nonlinear equation system, if the diffusion coefficient D_b depends on u_b. Let us introduce the following Kirchhoff transformation [26]

$$T : u_b \mapsto \psi = \int_0^{u_b} D_b(\tilde{u_b})\, \mathrm{d}\tilde{u_b}, \tag{3.1}$$

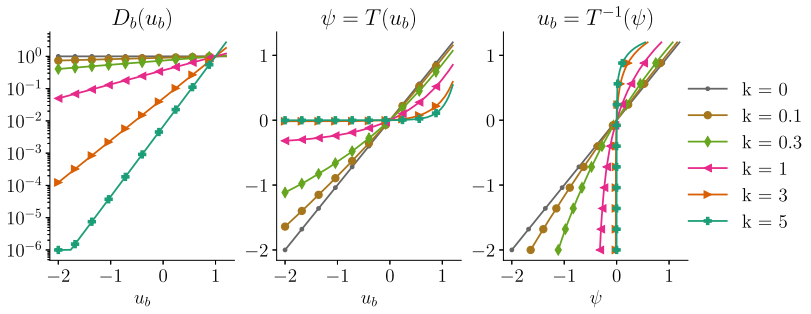

Fig. 3. An exponential diffusion coefficient function. Used for model verification tests in this work. The diffusion coefficient is given by $D_b(u_b) = \max(D_0 \exp\{k(u_b - 1)\}, D_{\min})$, where $D_0 = 1$, and $D_{\min} = 1 \times 10^{-6}$. The middle and right plot show the Kirchhoff transformation, $T(u_b)$, as defined in Eq. (3.1) and its inverse function, $T^{-1}(\psi)$. The analytical expressions for $T(u_b)$ and $T^{-1}(\psi)$ are given in Appendix A.

and we define $\hat{\psi}$ analogously in terms of $\hat{u}_b$. The chain rule yields

$$\nabla\psi = D_b(u_b)\nabla u_b, \tag{3.2}$$

which allows us to rewrite the left-hand-side of Eq. (2.1a),

$$-\nabla \cdot \nabla\psi = q\Phi_\Lambda, \tag{3.3}$$

in terms of the transformed variable ψ. Note that the left-hand-side is now a linear operator, and the nonlinearity is contained in the source term

$$q = -|P|\gamma(\Pi_P T^{-1}(\hat{\psi}) - u_e), \tag{3.4}$$

in terms of the inverse Kirchhoff transformation. This is an essential step, since Eq. (3.3) can be solved analytically in a simple radially-symmetric setting, cf. Section 3.2.

Remark 4. Since D_b is assumed positive and continuous, T is a strictly monotonically increasing function and we can uniquely define its inverse, T^{-1}. However, depending on the choice of $D_b(u_b)$, the image of T can be a strict subset (ψ_c, ∞) of $\mathbb{R}$, and consequently T^{-1} may be only defined on (ψ_c, ∞) [26]. This means not all solutions ψ of Eq. (3.3) have corresponding solutions u_b. For example, for the exponential function $D_b = D_0 \exp\{k(u_b - 1)\}$ and $k \in \mathbb{R}^+$, a function that fulfills our preconditions on D_b and that we will use subsequently in numerical verification tests, this is indeed the case. There, ψ_c corresponds to $u_b = -\infty$ and is well-defined. Nevertheless, T^{-1} is typically ill-conditioned around ψ_c (unbounded derivatives). This is evident in Fig. 3 for $k = 5$ where it becomes clear that the derivative can get arbitrarily large. (The same holds true for the Van Genuchten-Mualem model commonly used for the permeability in root-soil interaction, see Fig. 12 at $\theta_r\theta_s^{-1}$ in Section 4.4.)

Proposition. *Fortunately, this singularity disappears in the non-degenerate case [26]*

$$D_b(u_b) \geq D_{min} \quad \textit{for some} \quad D_{min} > 0. \tag{3.5}$$

In this case both T and T^{-1} are defined on all of $\mathbb{R}$. For instance, this property can be achieved for the exponential function D_b by using D_{min} as its lower bound, i.e. $D_b := \max(D_0 \exp\{k(u_b - 1)\}, D_{min})$.

The functions shown in Fig. 3 are regularized in this way using $D_{\min} = 1 \times 10^{-6}$ (see $k = 5$).

3.2. Local cylinder model and interface reconstruction

Firstly, let us consider an infinitely long straight cylinder of radius R embedded in an infinite domain $\Omega_\infty \subset \mathbb{R}^3$ with u_e being a given constant. Solving problem (2.1) then reduces to finding radially symmetric solutions by solving

$$-\frac{1}{r}\frac{\partial}{\partial r}\left(rD_b(u_b)\frac{\partial u_b}{\partial r}\right) = q(u_e, \hat{u}_b^{\bigcirc})\Phi_\Lambda, \tag{3.6}$$

on a cross-sectional plane in local cylinder coordinates. By using the Kirchhoff transformation, Eq. (3.1), and the definition of $\hat{u}_b^{\bigcirc}$, Eq. (1.3), we obtain

$$-\frac{1}{r}\frac{\partial}{\partial r}\left(r\frac{\partial\psi}{\partial r}\right) = q(u_e, \Pi_P T^{-1}(\hat{\psi}))\Phi_\Lambda. \tag{3.7}$$

As discussed above, q is now a nonlinear function of $\hat{\psi}$ (which solves Eq. (3.7) for $\varrho \to 0$). Using the uniform distribution kernel, Eq. (2.3), which is only non-zero in the local support region defined by the kernel radius ϱ, we obtain an analytical solution,

$$\psi(r) = \begin{cases} \hat{\psi}^{\bigcirc} - \frac{q}{2\pi}\left[\frac{r^2}{2\varrho^2} + \ln\left(\frac{\varrho}{R}\right) - \frac{1}{2}\right] & r \leq \varrho \\ \hat{\psi}^{\bigcirc} - \frac{q}{2\pi}\left[\ln\left(\frac{r}{R}\right)\right] & r > \varrho, \end{cases} \tag{3.8}$$

in terms of the transformed variable ψ and

$$\hat{\psi}^{\bigcirc} := \Pi_P \hat{\psi} \overset{\varrho \leq R}{=} \Pi_P \psi. \tag{3.9}$$

We refer to [18] for more details about the construction of the analytical solution (3.8).

Continuing in this setting and evaluating Eq. (3.8) at $r = \delta$, where $0 \leq \delta < \varrho$ denotes a distance to some point close to the tube centerline ($r = 0$), yields

$$\hat{\psi}^{\bigcirc} = \psi_\delta + \frac{q}{2\pi}\left[\frac{\delta^2}{2\varrho^2} + \ln\left(\frac{\varrho}{R}\right) - \frac{1}{2}\right], \tag{3.10}$$

where we introduced the symbol $\psi_\delta := \psi(r = \delta)$. We note that we evaluated ψ in the region regularized by the source distribution kernel. Moreover, recall that the coupling source term is given by

$$q = -|P|\gamma(\hat{u}_b^{\bigcirc} - u_e), \tag{3.11}$$

and with the Kirchhoff transformation and radial symmetry, we know that

$$\psi_\delta = T(u_{b,\delta}) \quad \text{and} \quad \hat{\psi}^{\bigcirc} = \Pi_P \hat{\psi} = T(\Pi_P \hat{u}_b) = T(\hat{u}_b^{\bigcirc}). \tag{3.12}$$

Result 1. *If we can estimate $u_{b,\delta}$ (for example by the discrete cell value in a finite volume discretization), we can find the interface pressure $\hat{u}_b^{\bigcirc}$ by solving a nonlinear equation composed of Eqs. (3.10) to (3.12),*

$$T(u_{b,\delta}) - T(\hat{u}_b^{\bigcirc}) - \frac{|P|\gamma}{2\pi}\left[\frac{\delta^2}{2\varrho^2} + \ln\left(\frac{\varrho}{R}\right) - \frac{1}{2}\right]\left(\hat{u}_b^{\bigcirc} - u_e\right) = 0, \tag{3.13}$$

which then allows to compute the source term q, given by Eq. (3.11). This means that an accurate approximation of $u_{b,\delta}$ and u_e is sufficient to compute a good approximation of $q(\hat{u}_b^{\bigcirc}, u_e)$.

This also suggests that we can indeed solve problem (2.1) instead of problem (1.1) while retaining a good approximation of q, u_e and $\hat{u}_b$ (for $r > \varrho$).

Remark 5. In the case that D_b is a constant, Eq. (3.13) can be explicitly solved for $\hat{u}_b^{\bigcirc}$ as shown in [18].

Remark 6. To see that Eq. (3.13) has a unique solution, it is sufficient to show that the expression on the left side is monotone with respect to $\hat{u}_b^{\bigcirc}$. In general, this only holds under some conditions. First, we assume that the kernel radius is chosen large enough such that $\ln\left(\frac{\varrho}{R}\right) \geq 0.5$. With this assumption, the third term is a monotonically decreasing (linear) function of $\hat{u}_b^{\bigcirc}$. Due to the assumption of positive diffusion coefficients, the functional $-T$ is also monotonically decreasing. It follows the monotonicity of the entire left hand side expression in Eq. (3.13) (constant terms do not influence the monotonicity), and Eq. (3.13) therefore has a unique solution.

For the general three-dimensional case, the second equality in Eq. (3.12) is only an approximation. The equality holds here due to the radial symmetry of the solution. This condition is violated in the presence of multiple arbitrarily-oriented tubes as they readily occur in tubular network structures (microvasculature, root systems, fiber networks). We motivate in the next section why this error is expected to be small.

3.3. Multiple interacting parallel tubes

Let us consider the case of many parallel tubes where the solution u_b only varies linearly along the tubes. Hence, we can consider a two-dimensional cross-sectional plane and denote with $\boldsymbol{x} \in \mathbb{R}^2$ a position on this plane. Due to the linearity of the Laplace operator in Eq. (3.3), we can obtain a general solution for ψ by superposition

$$\psi = \sum_{j=1}^{N} \psi_j + H, \quad \psi_j = -q_j f_j(\boldsymbol{x}), \tag{3.14}$$

where H is some harmonic function (for example chosen such that the boundary conditions are satisfied),

$$q_j = -|P_j|\gamma_j(\hat{u}^{\bigcirc}_{b,j} - u_e(\boldsymbol{x}_j)), \tag{3.15}$$

$$f_j(\boldsymbol{x}) = \begin{cases} \frac{1}{2\pi}\left[\frac{||\boldsymbol{x}-\boldsymbol{x}_j||_2^2}{2\varrho_j^2} + \ln\left(\frac{\varrho_j}{R_j}\right) - \frac{1}{2}\right] & ||\boldsymbol{x}-\boldsymbol{x}_j||_2 \le \varrho_j, \\ \frac{1}{2\pi}\left[\ln\left(\frac{||\boldsymbol{x}-\boldsymbol{x}_j||_2}{R_j}\right)\right] & \text{else.} \end{cases} \tag{3.16}$$

We remark that $\hat{u}^{\bigcirc}_{b,j}$ in q_j depends on contributions from all partial solutions ψ_j. To simplify notation, we assume $\varrho_i \le R_i$ in the following ($\hat{u}^{\bigcirc}_{b,i} = \Pi_{P_i}\hat{u}_b = \Pi_{P_i}u_b$). Applying the linear averaging operator (defined in Eq. (1.2)) on both sides of Eq. (3.14) and assuming that the tubes do not overlap yields

$$\begin{aligned} \Pi_{P_i}\psi &= \Pi_{P_i}\psi_i + \sum_{j=1, j\neq i}^{N} \psi_j(\boldsymbol{x}_i) + H(\boldsymbol{x}_i) \\ &= \Pi_{P_i}\psi_i + \psi(\boldsymbol{x}_i) - \psi_i(\boldsymbol{x}_i), \end{aligned} \tag{3.17}$$

where we used the mean value theorem for harmonic functions, i.e. $\Pi_{P_i}\psi_j = \psi_j(\boldsymbol{x}_i)$. From this, it follows that

$$\begin{aligned} \psi(\boldsymbol{x}_i) - \Pi_{P_i}\psi &= \psi_i(\boldsymbol{x}_i) - \Pi_{P_i}\psi_i \\ &= q_i(\Pi_{P_i}f_i - f_i(\boldsymbol{x}_i)) \\ &= |P_i|\gamma_i(\hat{u}^{\bigcirc}_{b,i} - u_e(\boldsymbol{x}_i))(f_i(\boldsymbol{x}_i) - \Pi_{P_i}f_i) \\ &= |P_i|\gamma_i(\hat{u}^{\bigcirc}_{b,i} - u_e(\boldsymbol{x}_i))f_i(\boldsymbol{x}_i), \end{aligned} \tag{3.18}$$

since the source term q_i is independent of $\boldsymbol{x}_i$ and $\Pi_{P_i}f_i = 0$. Finally, assuming that

$$\Pi_{P_i}\psi = \Pi_{P_i}T(u_b) \approx T(\Pi_{P_i}u_b) = T(\hat{u}^{\bigcirc}_b), \tag{3.19}$$

yields the reconstruction equation

$$T(u_b(\boldsymbol{x_i})) - T(\tilde{u}^{\bigcirc}_{b,i}) - |P_i|\gamma_i(\tilde{u}^{\bigcirc}_{b,i} - u_e(\boldsymbol{x_i}))f_i(\boldsymbol{x}_i) = 0, \tag{3.20}$$

which is equivalent to Eq. (3.13) with $\delta = 0$. The $\tilde{u}^{\bigcirc}_{b_i} \approx \hat{u}^{\bigcirc}_{b,i}$ resulting from solving Eq. (3.20) is an approximation due to Eq. (3.19). This extends our result from the single vessel case to multiple parallel vessels, but with the introduction of some approximation error due to the nonlinearity of D_b. Since Eq. (3.20) only requires point evaluations of u_b, the result extends to $\varrho_i > R_i$ as long as the kernel support regions do not overlap.

3.3.1. Error estimate for the approximation of the average operator

In the following, we estimate the error associated with approximation (3.19) in the reconstruction of the interface unknown. Let us assume that $\psi(\boldsymbol{x}_i)$ and $u_e(\boldsymbol{x}_i)$ are given and denote with u_b the exact solution. Again, to simplify notation, we assume $\varrho_i \le R_i$. Subtracting Eq. (3.18) from Eq. (3.20) yields

$$\Pi_{P_i}\psi - T(\tilde{u}^{\bigcirc}_{b,i}) = F_i(\hat{u}^{\bigcirc}_{b,i} - \tilde{u}^{\bigcirc}_{b,i}), \tag{3.21}$$

where $F_i := -|P_i|\gamma_i f_i(\boldsymbol{x}_i) \ge 0$. Assuming that $D_b \in C^1(U)$ (i.e. $T \in C^2(U)$), for some $U \subset \mathbb{R}$ such that $u_b(\Omega) \subset U$, and using Taylor's Theorem results in

$$\psi = T(u) = T(\hat{u}^{\bigcirc}_{b,i}) + T'(\hat{u}^{\bigcirc}_{b,i})(u - \hat{u}^{\bigcirc}_{b,i}) + \int_{\hat{u}^{\bigcirc}_{b,i}}^{u} T''(\tilde{u})(u - \tilde{u})\,\mathrm{d}\tilde{u}, \tag{3.22}$$

for any $u \in U$. Inserting the exact solution and applying the averaging operator on both sides give

$$\Pi_{P_i}\psi = T(\hat{u}^{\bigcirc}_{b,i}) + \Pi_{P_i}\left(\int_{\hat{u}^{\bigcirc}_{b,i}}^{u_b} T''(\tilde{u})(u_b - \tilde{u})\,\mathrm{d}\tilde{u}\right), \tag{3.23}$$

and inserting this expression into Eq. (3.21) results in

$$F_i(\hat{u}^{\bigcirc}_{b,i} - \tilde{u}^{\bigcirc}_{b,i}) = T(\hat{u}^{\bigcirc}_{b,i}) - T(\tilde{u}^{\bigcirc}_{b,i}) + \Pi_{P_i}\left(\int_{\hat{u}^{\bigcirc}_{b,i}}^{u_b} T''(\tilde{u})(u_b - \tilde{u})\,\mathrm{d}\tilde{u}\right). \tag{3.24}$$

The above equation can be equivalently written as

$$\int_{\hat{u}^{\bigcirc}_{b,i}}^{\tilde{u}^{\bigcirc}_{b,i}} (T'(\tilde{u}_b) - F_i)\,\mathrm{d}\tilde{u}_b = \Pi_{P_i}\left(\int_{\hat{u}^{\bigcirc}_{b,i}}^{u_b} T''(\tilde{u})(u_b - \tilde{u})\,\mathrm{d}\tilde{u}\right). \tag{3.25}$$

By assuming that there exists some constant $\tilde{C}_i$, independent of R_i, such that

$$\left|\int_{\hat{u}^{\bigcirc}_{b,i}}^{\tilde{u}^{\bigcirc}_{b,i}} (T'(\tilde{u}_b) - F_i)\,\mathrm{d}\tilde{u}_b\right| \geq \tilde{C}_i\left|\tilde{u}^{\bigcirc}_{b,i} - \hat{u}^{\bigcirc}_{b,i}\right|, \tag{3.26}$$

which for example holds if $D_b^{-1}(F_i) \notin [\min(\tilde{u}^{\bigcirc}_{b,i}, \hat{u}^{\bigcirc}_{b,i}), \max(\tilde{u}^{\bigcirc}_{b,i}, \hat{u}^{\bigcirc}_{b,i})]$, it holds that

$$\begin{aligned}
\tilde{C}_i\left|\tilde{u}^{\bigcirc}_{b,i} - \hat{u}^{\bigcirc}_{b,i}\right| &\leq \left|\Pi_{P_i}\left(\int_{\hat{u}^{\bigcirc}_{b,i}}^{u_b} T''(\tilde{u})(u_b - \tilde{u})\,\mathrm{d}\tilde{u}\right)\right| && (3.27)\\
&\leq 0.5\|D_b'\|_{L^\infty(u_b(P_i))}\Pi_{P_i}(u_b - \hat{u}^{\bigcirc}_{b,i})^2 && (3.28)\\
&\leq 0.5\|D_b'\|_{L^\infty(u_b(P_i))}(\operatorname{ess\,sup}_{P_i} u_b - \operatorname{ess\,inf}_{P_i} u_b)^2. && (3.29)
\end{aligned}$$

If the solution u_b is sufficiently smooth (e.g. C^1 or Lipschitz continuous), we deduce from the inequality above that the error introduced by the approximation $\tilde{u}^{\bigcirc}_{b,i}$ is $\mathcal{O}(R_i^2)$. Furthermore, it also shows that there is no error if $D_b = \text{const.}$, i.e. Eq. (2.1a) is a linear diffusion equation, or if u_b is constant on P_i (i.e. radial symmetric solution).

Remark 7. In a numerical scheme, the exact solution ψ is approximated by some discrete solution ψ_h, for which it holds that $|\psi(\boldsymbol{x}_i) - \psi_h(\boldsymbol{x}_i)| = \mathcal{O}(h^2)$ (h denotes the discretization length, see Section 4) when using a second order scheme. Therefore, the approximation $\psi_h(\boldsymbol{x}_i) \approx \psi(\boldsymbol{x}_i)$ introduces an error of $\mathcal{O}(h^2)$, whereas the error introduced by the approximation $\Pi_{P_i}\psi \approx T(\hat{u}^{\bigcirc}_{b,i})$ is in the order of $\mathcal{O}(R_i^2)$. This suggests that on grids where $h > R_i$, $\Pi_{P_i}\psi \approx T(\hat{u}^{\bigcirc}_{b,i})$ yields a good approximation, without being the main source of error. This result is supported by the numerical results in Section 4. Since the goal of the kernel method is to allow coarser grids by choosing kernel support radii $\varrho > R_i$ while maintaining accuracy [18], grid resolutions with $h > R_i$ correspond to the typical use case.

3.4. Multiple arbitrarily-oriented tubes

The numerical method introduced above for single or parallel tubes can also be applied for the general three-dimensional case with arbitrarily-oriented tubes. However, for arbitrarily-oriented tubes an additional error is introduced because the mean value property of harmonic functions, used for ψ_j to derive Eq. (3.18), is no longer valid.

The additional error depends on $|\Pi_{P_i}\psi_j - \psi_j(\boldsymbol{x}_i)| = |q_j||\Pi_{P_i} f_j - f_j(\boldsymbol{x}_i)|$, with $j \neq i$ and f_j as defined in Eq. (3.16). Assuming that the kernel support regions are non-overlapping, we apply Taylor's Theorem to deduce the following estimate

$$|\Pi_{P_i} f_j - f_j(\boldsymbol{x}_i)| \leq \frac{C}{2}R_i^2. \tag{3.30}$$

Assuming that a contribution of another tube has the shape of a line source, the constant C can be computed, yielding

$$|\Pi_{P_i} f_j - f_j(\boldsymbol{x}_i)| \leq \frac{R_i^2}{4\pi(\|\boldsymbol{x}_i - \mathcal{E}_j^{\perp}(\boldsymbol{x}_i)\|_2 - R_i)^2}, \tag{3.31}$$

where $B_{R_i}(\boldsymbol{x}_i)$ denotes a ball of radius R_i centered at $\boldsymbol{x}_i$, and $\mathcal{E}_j^{\perp}$ orthogonally projects $\boldsymbol{x}$ onto the centerline of tube j. The derivation of the estimate is given in Appendix B. We note that most other tubes in a large network system embedded in Ω are far away from the segment i, and therefore the error is small. Close tubes may cause a signification error. However,

average distances to the closest neighbor tube in relevant applications are often $10R_i$ and larger. With these estimates and by using similar arguments as in Section 3.3.1, we conclude that also for the case of arbitrarily-oriented tubes, the error introduced by reconstructing $\tilde{u}^{\bigcirc}_{b,i}$ from Eq. (3.20) using approximation (3.19) is not dominant on grids where $h > R_i$. This conclusion is supported by numerical experiments, e.g. [23].

Finally, the line segments in practical networks are finite and kinks and bifurcations may introduce additional errors since there the kernel support regions of two connected vessels may overlap and the assumption of discrete cylinders as segments may result in errors in the estimation of the network surface area. In [23], the author proposes a numerical method that does not suffer from these errors since the tube interface is explicitly resolved by the three-dimensional computational mesh. It is shown that the approximation of kinks and bifurcations with cylinder segments do not introduce significant errors and that these errors are irrelevant in practical simulations of tissue perfusion or root water uptake.

4. Numerical results and discussion

In this section, we investigate numerically convergence properties of the introduced method and the influence of its numerical parameters, in particular, the kernel width ϱ and the reconstruction distance parameter δ, on the approximation error. Moreover, we investigate which model errors are involved with relaxing the assumptions under which Result 1 was derived in Section 3.2, concluding with a root water uptake simulation.

The three-dimensional bulk domain Ω and the network domain Λ are spatially decomposed into the meshes Ω_h and Λ_h consisting of control volumes (cells) $K_\Omega \in \Omega_h$ and $K_\Lambda \in \Lambda_h$, respectively. The discretization length, i.e. the maximum cell diameter, is denoted as h. To discretize the nonlinear diffusion problem (2.1) in space, a cell-centered finite volume method with a two-point flux approximation is employed [18]. The resulting nonlinear system of equations is solved with Newton's method. To solve the learnized system of equations within each Newton iteration, we use the same linear solver as described in [18], that is, a stabilized bi-conjugate gradient method with a block-diagonal incomplete LU-factorization-based preconditioner. All presented methods and simulations are implemented using the open-source software framework DuMu$^{\text{x}}$ [27] with the network grid implementation `dune-foamgrid` [28] for representing the embedded network domain.

For general nonlinear constitutive models (e.g. the Van Genuchten curves in Section 4.4), the Kirchhoff transformation Eq. (3.3) and its inverse are computed numerically. Here, we use numerical integration based on the double exponential transformation [29] and Brent's method for the inverse transformation. For fast evaluation of the inverse transformation, the functional $T^{-1}(\psi)$ is replaced by a lookup table with local linear interpolation and a high sampling rate. The nonlinear interface reconstruction, Eq. (3.13) (single tube) or Eq. (3.20) (multiple tubes), is solved using Brent's method. For the numerical integration routine used for the distributed source terms in the three-dimensional case, we refer the interested reader to [18].

4.1. Analytical solutions for multiple parallel tubes

In this section, we derive for the verification of the introduced method, two types of analytical solutions based on the superposition of point source solutions. We consider an infinite two-dimensional domain $\Omega \subset \mathbb{R}^2$ that cuts through N parallel non-overlapping circular tubes of different radii R_i. The flow resistance that the tubes pose to flow through Ω and its volume are neglected so that Ω can be extended inside the tube radius and comprises the entire plane without circular cut-outs.

The error involved with this assumption has been numerically analyzed in [23] and found to be small. The assumption is also commonly used in 1d-3d models [30,31,5,2,32,3,33,18] based on the underlying assumption that tube radii are small. As noted in the beginning of this section, an analytical solution for ψ can be obtained by superposition, see Eq. (3.14). The analytical solution for u_b is then found by numerical or exact inversion of the Kirchhoff transformation.

In the following, we compute the coefficients of such solutions numerically for given tube center positions $\boldsymbol{x}_i$, tube radii R_i, and $u_{e,i}$, fixed γ_i, given $D_b(u_b)$, and $\varrho_i \geq R_i$. For a fully determined analytical solution, we require N average interface unknowns $\hat{u}^{\bigcirc}_{b,i}$, and some constant C_ψ (corresponds to the choice $H \equiv C_\psi$ in Eq. (3.14)). Furthermore, we have N equations

$$\hat{u}^{\bigcirc}_{b,i} = \frac{1}{|P_i|}\int_{P_i} T^{-1}(\psi(\boldsymbol{x}))\,\mathrm{d}\boldsymbol{x} \approx \sum_{k=1}^{K_{\text{ip}}} T^{-1}(\psi(\boldsymbol{x}_{i,k}))\,w_{i,k}, \tag{4.1}$$

where $\boldsymbol{x}_{i,k} \in \mathbb{R}^2$, $w_{i,k} \in \mathbb{R}^+$ are K_{ip} integration points and weights. We choose $\boldsymbol{x}_{i,k}$ to be uniformly distributed on P_i. To compute the solution numerically, we choose $\hat{u}^{\bigcirc}_{b,1}$ and then solve Eq. (4.1) with a Newton method, where in every step the dense linear system

$$\begin{bmatrix} \frac{\partial r_1}{\partial C_\psi} & \frac{\partial r_1}{\partial u_1} & \cdots & \frac{\partial r_1}{\partial u_N} \\ \frac{\partial r_2}{\partial C_\psi} & \frac{\partial r_2}{\partial u_1} & & \\ \vdots & & \ddots & \\ \frac{\partial r_N}{\partial C_\psi} & & & \frac{\partial r_N}{\partial u_N} \end{bmatrix} \begin{bmatrix} \Delta C_\psi \\ \Delta u_2 \\ \vdots \\ \Delta u_N \end{bmatrix} = \begin{bmatrix} r_1 \\ r_2 \\ \vdots \\ r_N \end{bmatrix}, \tag{4.2}$$

is solved, where u_i is short notation for $\hat{u}^{\bigcirc}_{b,i}$ and

$$r_i = \hat{u}^{\bigcirc}_{b,i} - \sum_{k=1}^{K_{\text{ip}}} T^{-1}(\psi(\boldsymbol{x}_{i,k}))w_{i,k} = 0, \tag{4.3}$$

are the nonlinear residuals. The partial derivatives are approximated by numerical differentiation. The resulting solution is denoted as U_b.

In a variation of the above algorithm we use

$$\tilde{r}_i = \tilde{u}^{\bigcirc}_{b,i} - T^{-1}\left(\sum_{k=1}^{K_{\text{ip}}} \psi(\boldsymbol{x}_{i,k})w_{i,k}\right) = 0, \tag{4.4}$$

and the resulting solution is denoted as $\tilde{U}_b$. This variation exactly corresponds to the approximation (3.19). We will show in the subsequent numerical experiments that a distributed source scheme with an interface reconstruction based on Eq. (3.20) in a setup corresponding to the two-dimensional parallel tube setup converges to the modified solution $\tilde{U}_b$. However, U_b and $\tilde{U}_b$ are very similar so that the error $||U_b - \tilde{U}_{b,h}||$ for a numerical approximation $\tilde{U}_{b,h}$ is small in practice. Examples of U_b for three parallel tubes are shown Fig. 4.

4.2. Discrete error measures

To quantify the discretization errors, we define the following relative discrete L^2-errors for the unknown u_b, its transformed variable $\psi = T(u_b)$, and the source term q as

$$E_{u_b} = \frac{1}{u_{b,\text{ref}}}\left[\frac{1}{|\Omega_h|}\sum_{K_\Omega \in \Omega_h} |K_\Omega| \left(u_{b,K_\Omega} - U_{b,K_\Omega}\right)^2\right]^{\frac{1}{2}}, \tag{4.5}$$

where $u_{b,\text{ref}}$ is a constant reference value chosen as 1 (unless otherwise indicated) and u_{b,K_Ω} and U_{b,K_Ω} are the numerical and analytical solutions evaluated at the center of K_Ω;

$$E_{\psi} = \frac{1}{\psi_{\text{ref}}}\left[\frac{1}{|\Omega_h|}\sum_{K_\Omega \in \Omega_h} |K_\Omega| \left(\psi_{K_\Omega} - \Psi_{K_\Omega}\right)^2\right]^{\frac{1}{2}}, \tag{4.6}$$

where ψ_{ref} is chosen as 0.1 (unless otherwise indicated), and

$$E_{q} = \frac{1}{q_{\text{ref}}}\left[\frac{1}{|\Lambda_h|}\sum_{K_\Lambda \in \Lambda_h} \left(q_{K_\Lambda} - Q_{K_\Lambda}\right)^2\right]^{\frac{1}{2}}, \tag{4.7}$$

where q_{K_Λ} and Q_{K_Λ} are the numerical and the exact source for the tube segment K_Λ, defined as the integral of q in Eq. (2.1a) over K_Λ and $q_{\text{ref}} = \max_{K_\Lambda \in \Lambda_h} |Q_{K_\Lambda}|$. Finally, we analogously define relative discrete L^2-errors with respect to the modified analytical solution $\tilde{U}$ (see Section 4.1), and accordingly denote them as $\tilde{E}_{u_b}$, $\tilde{E}_{\psi}$, $\tilde{E}_{q}$. We note that all errors are reported against the regularized solution u_b rather than the line source solution $\hat{u}_b$. The exact solutions for u_e and q are equivalent in both settings.

4.3. Grid convergence tests

In the following, we present grid convergence tests against the analytical solution for a single tube and against the analytical solutions of Section 4.1 for multiple parallel tubes. The diffusion coefficient $D_b(u_b)$ is chosen as exponential function shown in Fig. 3 with $D_0 = 0.5$. Analytical expressions for the Kirchhoff transformation and its inverse are given in Appendix A. The diffusive wall permeability γ is chosen as 1.

As motivated in Section 4.1, we expect that the numerical solution converges to the modified solution $\tilde{U}_b$. However, U_b and $\tilde{U}_b$ are expected to be very similar. They are identical for a single infinite tube, where the approximation (3.19) is exact.

4.3.1. Single tube convergence rates

Let us consider Eq. (2.1a) for an infinite straight tube with constant u_e embedded in an infinite bulk domain. The problem reduces to solving Eq. (3.6). The analytical solution is given by Eq. (3.8). Note that for this radially symmetric case Eq. (3.19) is exact. We therefore only report errors with respect to U_b since U_b and $\tilde{U}_b$ (as described in Section 4.1) are identical for

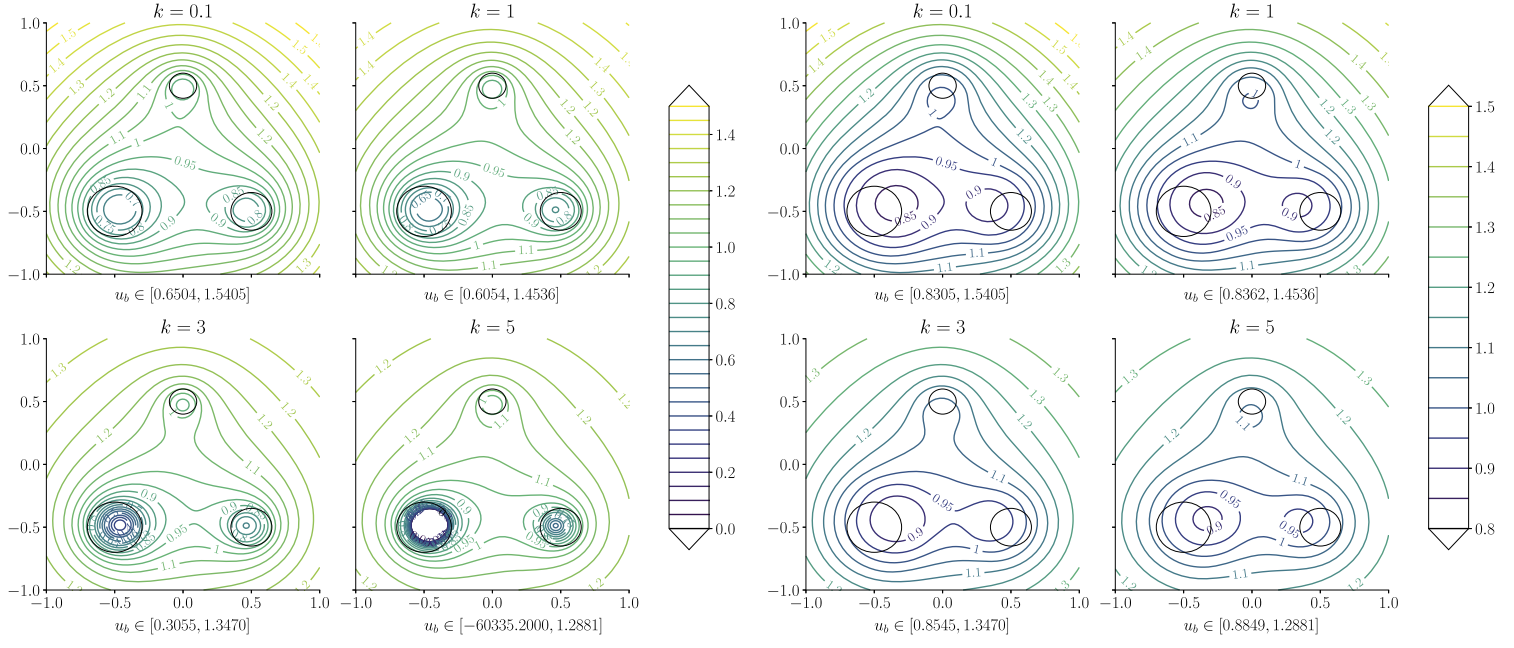

Fig. 4. Contour plot of the analytical solution U_b for three parallel tubes. Cross-sectional perimeter shown by black circles. Plotted for tube radii $R = (0.2, 0.15, 0.1)$, $\varrho_i = R_i$ (left) and $\varrho_i = 2R_i$ (right), and various exponential diffusion coefficient functions (Fig. 3, $D_0 = 0.5$). The higher k the larger the gradients at the tube-bulk interface (denser contour lines). The scale is cut off at $u_b = 0$ (hence the white hole in the biggest tube for $k = 5$). The minimum and maximum values of u_b are given under each plot. Note that due to the large gradients in the case $k = 5$, $\varrho_i = R_i$ (left) the minimum of u_b is found to be -6×10^4. We therefore consider this case a hard-to-solve test case. We note that by increasing the kernel radius ϱ, u_b is mollified (left vs. right). The interface reconstruction algorithm needs to reconstruct the average u_b on the black line (tube-bulk interface) shown in the *left* figure, regardless of ϱ. The mollifier turns $\hat{u}_b$ (equivalent to u_b on the left figure outside the black circle) into a function that is much easier to approximate by numerical schemes. However, using the proposed algorithm, $\hat{u}_b$ can be reconstructed from u_b.

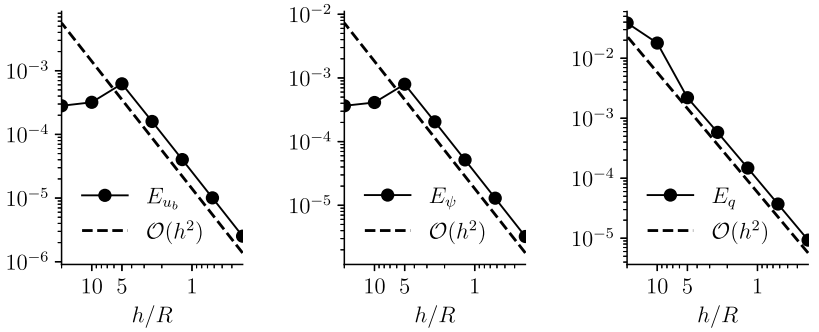

Fig. 5. Grid convergence of relative discrete errors for single infinite tube. The kernel radius is $\varrho = 5R$ and the tube radius $R = 0.01$. h is the discretization length. Following a pre-asymptotic range, second order convergence in all variables is observed for $h \leq \varrho$.

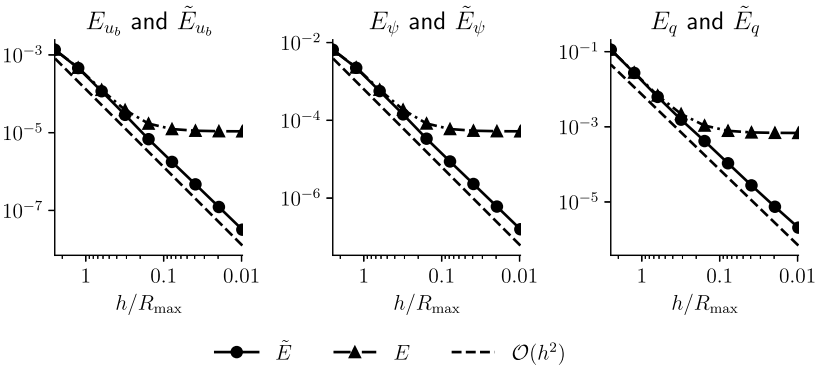

Fig. 6. Grid convergence for relative discrete errors E and $\tilde{E}$. The maximum tube radius is $R_{\max} = 0.2$ (the three tube radii are $0.2, 0.15, 0.1$), kernel radii are $\varrho_i = 2R_i$ and the exponential rate parameter is $k = 1$.

the single tube case. We choose $R = 0.01$, $\varrho = 0.05$, $\hat{u}_b^{\bigcirc} = 0.5$, $u_e = 0.1$, and numerically solve Eq. (3.6) on the unit interval with the analytical solution prescribed as Dirichlet boundary conditions at $r = 1$. The source term is computed based on u_e using the proposed interface reconstruction, Eq. (3.13).

Grid convergence results are shown in Fig. 5. The grid is uniformly refined, starting from $h = 20R$. Initially, we observe a pre-asymptotic range since the kernel support is not resolved by the grid yet. After the 3rd refinement, where $h = \varrho$, all errors decay quadratically with uniform grid refinement for all quantities, the primary variable u_b, the transformed variable ψ, and the numerical source term q. As observed by [18], the onset of second-order convergence is determined by the kernel radius rather than the tube radius. This allows for good control of the error even for simulations where fine grids are not feasible.

4.3.2. Multiple parallel tubes

Next, we consider a two-dimensional domain $\Omega = [-1, 1] \times [-1, 1]$ that perpendicularly cuts three tubes with radii $(R_{\max}, \frac{3}{4}R_{\max}, \frac{1}{2}R_{\max})$ centered at $\boldsymbol{x}_1 = (-0.5, -0.5)$, $\boldsymbol{x_2} = (0.5, -0.5)$, $\boldsymbol{x_3} = (0, 0.5)$, respectively. The tube unknowns $u_{e,i}$ are given by $(0.3, 0.2, 0.1)$ and the kernel radii are $(0.4, 0.3, 0.2)$, respectively. The average interface unknown of the largest tube $\hat{u}_{b,1}^{\bigcirc}$ is fixed as 0.8. The analytical solutions U_b and $\tilde{U}_b$ are computed as described in Section 4.1. The solution U_b is shown for different k in Fig. 4 for $\varrho_i = R_i$ and $\varrho_i = 2R_i$.

In the following, we investigate the influence of the exponential rate parameter k of $D_b(u_b)$ and the influences of the tube radii $R_{\max}$ on the discretization and the error involved in approximation Eq. (3.19). We compute grid convergence both against U_b and $\tilde{U}_b$. The mesh Ω_h is uniformly refined starting with 4×4 cells. On boundaries, we enforce the respective analytical solution as Dirichlet boundary condition for u_b.

In the first case, we set $k = 1$ and $R_{\max} = 0.2$. The errors E_{u_b}, E_ψ and E_q are shown in Fig. 6 with uniform grid refinement. As motivated in Section 4.1, we see convergence to the modified analytical solution $\tilde{U}_b$. Second-order convergence is observed for all relevant quantities. For the convergence test against U_b, we observe a non-reducible error. Due to the way the analytical solution is constructed, we can identify this error as the model error caused by approximation (3.19). However, most interestingly, this error is very small (less than 0.1% for $\tilde{E}_q$) in this case and shows only an influence in the convergence plot for grid discretization length below the tube radius, i.e. $h < R_{\max}$.

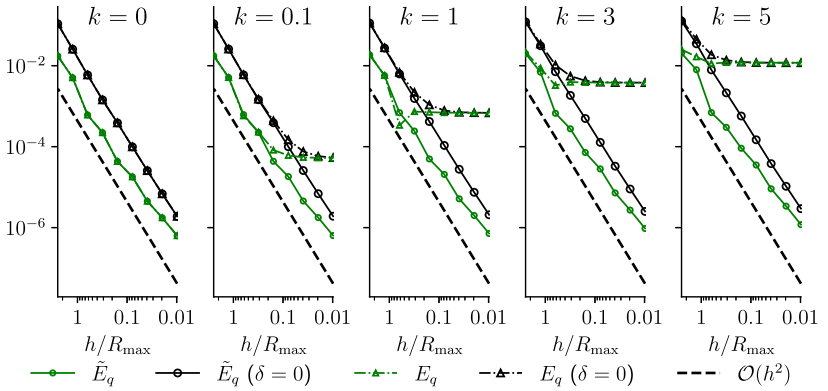

Fig. 7. Grid convergence of source errors for different exponential coefficients k. Source errors E_q and $\tilde{E}_q$ for $k = 0.1, 1, 3$ and 5 with $R = (0.2, 0.15, 0.1)$.

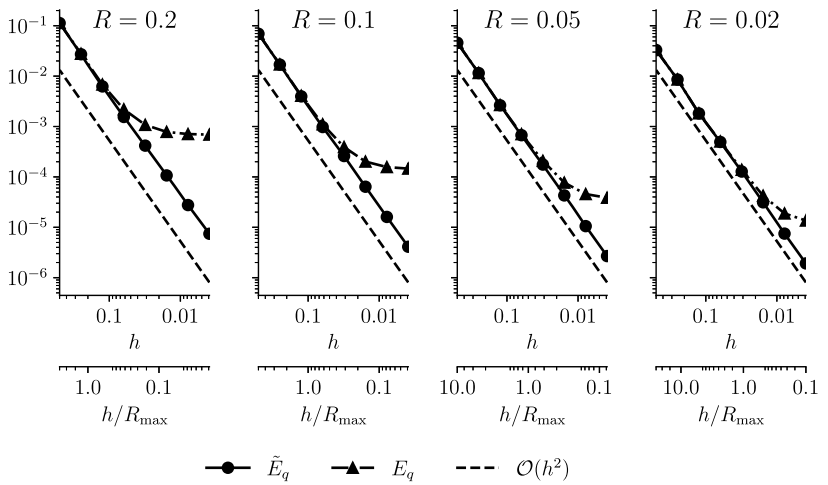

Fig. 8. Grid convergence of source errors for different tube radii R. Source errors E_q and $\tilde{E}_q$ with $k = 1$ and $R_{\max} = 0.2, 0.1, 0.05, 0.02$.

In the second case, we investigate more challenging cases by varying k, cf. Fig. 3. The source error for different k is shown in Fig. 7. As convergence of all three fields u_b, ψ, q is confirmed in Figs. 5 and 6, we only report errors for q in the following, allowing for a more concise presentation.

For $k = 0$ the exponential function reduces to a constant. Therefore, this case corresponds to the linear stationary diffusion equation analyzed in [18]. Due to the mean value theorem for harmonic functions, approximation (3.19) is exact and $U_b = \tilde{U}_b$. The larger k the stronger the changes in D_b. In particular, as shown in Fig. 4, the gradient of u_b at the tube interface is large for larger k and the value of u_b varies considerably along the tube perimeter. Nevertheless, the largest observed error for $k = 5$ is $E_q \approx 1\%$, and only dominates the discretization error for $h < R_{\max}$.

In a third case, we fix $k = 1$ and vary the tube radii $R_{\max} = 0.2, 0.1, 0.05$ and 0.02. The analytical solution is computed such that the source term of the largest tube is equivalent for all cases. The source errors are presented in Fig. 8. It is evident that the error due to approximation (3.19) decreases with smaller tube radius. This is in good agreement with the error estimate in Section 3.3.1. In particular, we can see again that the error is only relevant in comparison to the discretization error for $h < R_{\max}$.

4.3.3. *Influence of the kernel radius* ϱ

In the fourth test case, we investigate the influence of the kernel radius ϱ on the discretization error. Therefore, we choose a case where the approximation error due to Eq. (3.19) does not dominate the total model error. We choose $R_{\max} = 0.05$ and $k = 1$. The discretization length h is fixed at 0.125. All other parameters are the same as in Section 4.3.2. The kernel radius is increased from $2R_i$ to $12R_i$. The resulting source errors E_q with respect to the analytical solution U_b are shown in Fig. 9. The error decays with increasing kernel radius. Interestingly, the speed of this decay is comparable with the error decay by grid refinement and matches the observations in [18] for the linear diffusion equation. It can also be seen that as soon as the kernel regions of the largest two tubes start to overlap the source error increases again. The error decay is best explained by the better approximation of $u_b(\boldsymbol{x}_i)$ used in the reconstruction algorithm, cf. Eq. (3.13) and Eq. (3.20). Since u_b is increasingly regularized with increasing kernel support, it becomes easier to approximate the function numerically.

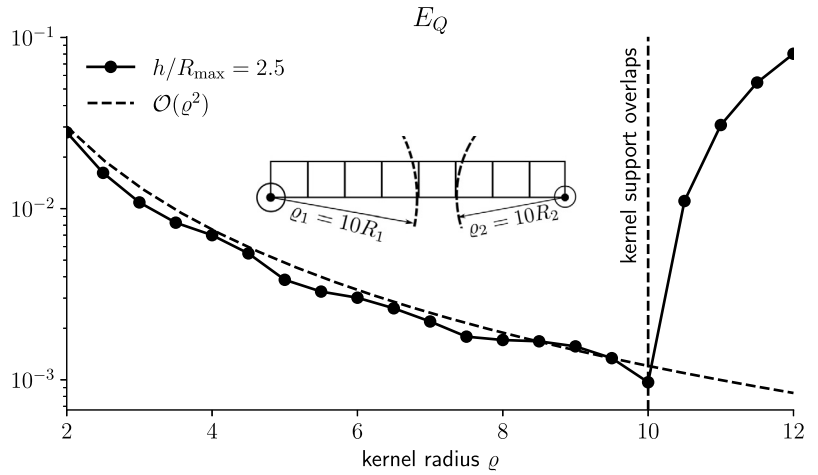

Fig. 9. Source errors E_q for different kernel radii ϱ. The maximum tube radius is $R_{\max} = 0.2$ and $k = 1$. Semi-logarithmic plot. Exact source terms Q_i are the same for all ϱ.

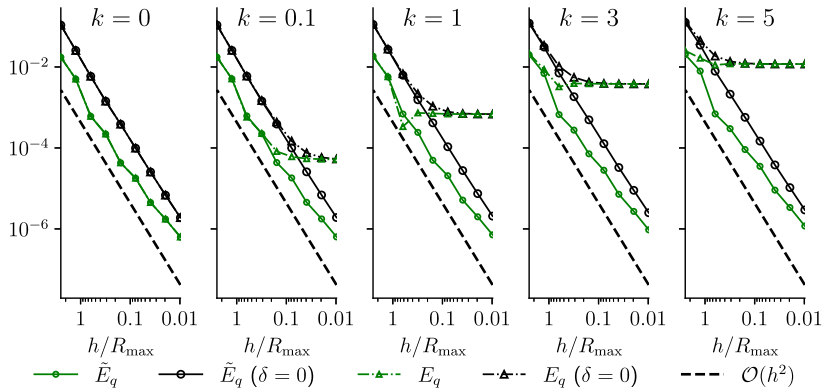

Fig. 10. Grid convergence of source errors with non-zero δ. Source errors E_q and $\tilde{E}_q$ for different exponential coefficients $k = 0.1, 1, 3$ and 5 with $R = (0.2, 0.15, 0.1)$, where δ is defined as the mean distance between the tube and bulk cell containing the tube (in green). $\delta = 0$ (in black) is the situation where the tube is located at the center of the bulk cell. (For interpretation of the colors in the figure(s), the reader is referred to the web version of this article.)

4.3.4. Discrete evaluations of $u_{b,\delta}$ or $u_{b,0}$

As noted in Section 3.2, the reconstruction allows to consider that the numerically measured quantity u_{b,K_Ω} in cell K_Ω does not represent the value on the centerline but rather a value in some distance δ. This is particularly relevant for coarse discretizations where it may make a difference whether the root segment is located in the middle or the corner of a 3D cell.

As a fifth case, we present the results of the second case (where u_{b,K_Ω} is interpreted as u_0) in comparison with results for which we assumed in the reconstruction that u_{b,K_Ω} represents the $u_{b,\delta}$ and δ is chosen as the mean minimum distance between tube segment and bulk cell [34],

$$\delta = \frac{1}{|K_\Omega|} \int_{K_\Omega} \min_{\boldsymbol{x}' \in K_\Lambda} ||\boldsymbol{x} - \boldsymbol{x}'||_2 \, \mathrm{d}\boldsymbol{x}. \tag{4.8}$$

The resulting source errors are shown in Fig. 10. We observe that the error is significantly reduced. As for the previous cases, the error curve flattens as soon as the error is dominated by the mean value approximation error.

4.4. Root–soil interaction scenario

In the following application scenario, we compute root water uptake with small root system architecture obtained from MRI measurements. The scenario is similar to benchmark scenario C1.2 presented in [35]. However, we solve a stationary problem for various root collar pressures enforced as Dirichlet boundary conditions at the root collar.

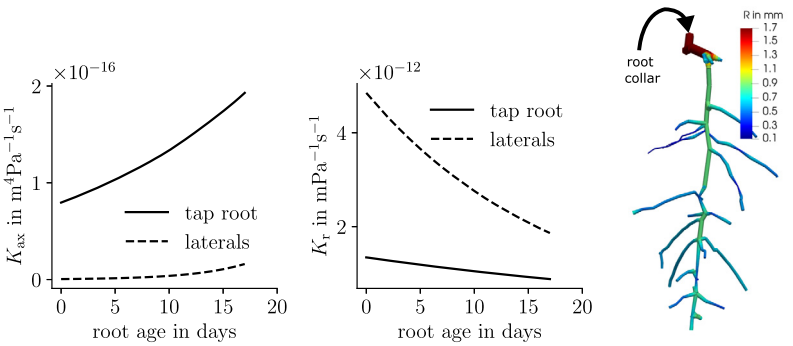

Fig. 11. Root conductivities and radius for a lupin root system. Left and middle, age-dependent hydraulic root conductivities from [35]. The axial root conductivity K_{ax} corresponds to D_e and the radial root conductivity K_{r} corresponds to γ in the nonlinear diffusion equation. Right, 8-day-old lupin root system reconstructed from MRI data (courtesy of M. Landl, FZ Jülich). Grid data available from [36]. The root segment radius is visualized to scale. The rooting depth is about 10 cm. Figure adapted from [37].

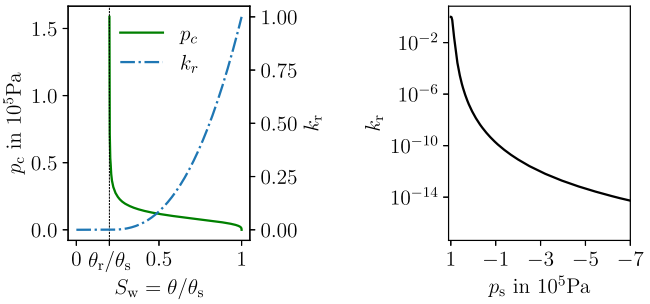

Fig. 12. Van Genuchten-Mualem model. Left, relative permeability k_r and capillary pressure p_c over water content θ using the Van Genuchten-Mualem model for a loamy soil, $K = 5.899\,12 \times 10^{-13}$ m^2, $\theta_r = 0.08$, $\theta_s = 0.43$, $\alpha = 4.077 \times 10^{-4}$ Pa^{-1}, $n = 1.6$. Right, the relative permeability k_r as a function of soil water pressure p_s. The term $\mu^{-1} K k_r(p_s)$ in the root-soil scenario corresponds to $D_b(u_b)$ in the general nonlinear diffusion model.

To make it easier for readers familiar with root-soil interaction, we introduce several symbols and relate them to the symbols in Eq. (2.1). The soil pressure p_s and root pressure p_r (in Pa) correspond to the unknowns u_b and u_e. The term $\mu^{-1} K k_r$ corresponds to D_b, where $\mu = 1 \times 10^{-3}$ Pa s is the viscosity of water, K (in m^2) is the intrinsic permeability of the solid matrix, and k_r is the dimensionless relative permeability. Relative permeability is commonly modeled as a nonlinear function of water content which in turn can be described by a nonlinear function of soil water pressure. The axial root conductivity K_{ax} (in m^4 Pa^{-1} s^{-1}) corresponds to D_e, and the radial root conductivity K_{r} (in m Pa^{-1} s^{-1}) corresponds to γ. We can then reformulate problem (2.1) to obtain a stationary root-water uptake model neglecting gravity,

$$-\nabla \cdot \left(\mu^{-1} k_r(p_s) K \nabla p_s\right) = q \Phi_\Lambda \qquad \text{in} \quad \Omega, \tag{4.9a}$$

$$-\partial_s \left(K_{\text{ax}} \partial_s p_r\right) = -q \qquad \text{on} \quad \Lambda, \tag{4.9b}$$

$$q = -2\pi R K_{\text{r}} (\hat{p}_s^{\bigcirc} - p_r), \tag{4.9c}$$

where $\hat{p}_s^{\bigcirc}$ denotes the average soil pressure at the root-soil interface.

Let $\theta = S_w \theta_s$ denote the water content, where S_w is the water saturation and θ_s is the water content at saturation (equal to the porosity of the soil), and let θ_r denote the residual water content. The relative permeability is modeled by the Van Genuchten-Mualem model [10,11]

$$\begin{aligned} k_r(S_e) &= S_e^{\lambda} [1 - (1 - S_e^{1/m})]^2, \\ S_e(p_c) &= \left((\alpha p_c)^n + 1\right)^{-m}, \\ p_c(p_s) &= -p_s, \end{aligned} \tag{4.10}$$

where p_c (in Pa) is called capillary pressure, $S_e = \theta_r \theta_s^{-1}$ and θ_r, θ_s, α, n, $m = 1 - n^{-1}$ are material-dependent parameters. In the following, we use a parametrization corresponding to loam given in [35], see Fig. 12. The functions in Eq. (4.10) are plotted in Fig. 12. The axial and radial root conductivities vary along the roots dependent on the root age. These root conductivity values are plotted in Fig. 11. For tabularized values, we refer to [35].

The root system shown in Fig. 11 is embedded in a box-shaped domain with dimension $8 \times 8 \times 15$ cm. The top of the box intersects with the root collar at $x_3 = 0$ cm. The bottom of the domain is located at $x_3 = -15$ cm. We prescribe a water

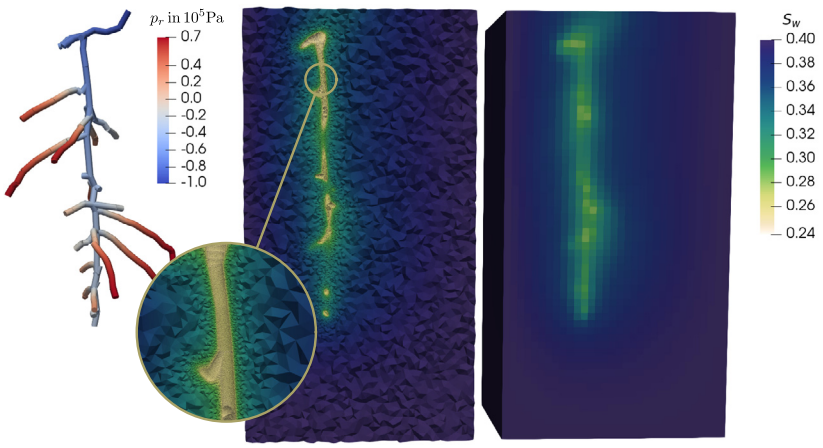

Fig. 13. Model comparison for root water uptake scenario. Simulation result for $p_{r,c} = -1 \times 10^5$ Pa. Left, root pressure distribution in the root. Right, vertical cut through the soil domain (a box of $8 \times 8 \times 15$ cm centered at $\boldsymbol{x} = (0, 0, -7.5)$ cm) in the $x_2 - x_3$-plane at $x_1 = 0.7$ cm. The left cut shows the soil saturation for a projection-based mixed-dimension method with fully resolved root-soil interface [PS]. The computational mesh has 12M cells and the average cell diameter of the smallest 10% of cells is $\bar{h}_{10} = 82$ µm. The right cut shows the corresponding saturation distribution for the new kernel-based mixed-dimension scheme [DS] on a mesh with 60k cells and $h_{\min} = 0.25$ cm.

saturation of $S_w = 0.4$ (corresponding to $p_s = 0.78 \times 10^5$ Pa) at all sides except for the top boundary where we enforce a zero-flow Neumann boundary condition. In the root domain, we prescribe no-flow boundary conditions at root tips and a fixed pressure $p_{r,c}$ at the root collar. We solve the same scenario for $p_{r,c} = 0.0, -0.5 \times 10^5, -1.0 \times 10^5, -2.5 \times 10^5$, and -5.0×10^5 Pa. With decreasing root pressure, the flow rate of water leaving the domain at the root collar (transpiration rate) increases and the root-soil interface dries out. Dry soil (low water saturation) corresponds to a strong decrease of the local hydraulic conductivity, cf. Fig. 12.

We compare the results obtained with the presented distribution kernel-based method (DS) for $\varrho_i = 3R_i$ and δ chosen as in Section 4.3.4 with two previously published methods. In [23] the root-soil interface is fully resolved by a locally refined unstructured three-dimensional mesh. The roots are modeled with Eq. (4.9b) on a network of line segments. The solution p_r (or u_e) is projected onto the closest surface on the three-dimensional mesh to evaluate a source term similar to Eq. (4.9c). Since the root-soil interface is resolved, this resolved-interface method (PS) does not suffer from the approximation errors described in the previous sections, however, this comes at a higher computational cost as we will demonstrate. Secondly, we compare the result to results obtained with the method presented in [3] and adapted for root-soil interaction as described in [34]. There, the source term is restricted to the tube-bulk interface, and the bulk interface unknown is obtained by an average over the tube perimeter. We abbreviate this method by CSS (cylindric surface source) in the following. All methods are implemented in a common software framework using DuMu$^{\text{x}}$ [27,34] and are therefore easily comparable. In fact they share most of the source code and mostly differ in the way the soil and root domain are coupled.

The simulation result for $p_{r,c} = -1 \times 10^5$ Pa and both methods PS and DS is shown in Fig. 13. A close-up shows the locally refined grid necessary to resolve the root-soil interface. Due to the regularizing effect of both the distribution kernel and the coarse grid the DS solution u_b does not contain the low saturation values found on the interface in the PS solution. Hence, the question is if these values can be accurately reconstructed from u_b. As a global measure of how accurate the source terms q are approximated, we compute the transpiration rate at the root collar. Due to mass conservation, the transpiration rate is given by

$$r_T = \int_\Lambda q(s)\,\mathrm{d}s. \tag{4.11}$$

Transpiration rates for all three methods and all root collar pressures are shown in Fig. 14. Firstly, it can be observed that the DS method approximates all transpiration rates with a maximum relative difference of 3% to the high fidelity PS solution, notably using a quite coarse grid ($h = 5$ mm). Using the same grid resolution the CSS method shows a difference of 10% for $p_{r,c} = 0$ Pa and even 60% for $p_{r,c} = -5 \times 10^5$ Pa. Since CSS is a consistent method the results improve with grid refinement. The difference to the reference solution is comparable to that of DS in terms of the transpiration rate only when using strong local grid refinement resulting in a mesh of 1.9M cells. Although the finest mesh used for the PS method in this work is locally refined with a total of 12M cells and well-resolved root-soil interface (cf. Fig. 13), the grid convergence results shown in the right-most plot in Fig. 14 suggest that the transpiration rate is not fully converged yet. Interestingly, following the trend, the transpiration rate is expected to get even closer to the solution of the DS method for which the computed transpiration rate is stable with grid refinement already for rather coarse grids.

Fig. 15 shows the reconstructed interface soil pressures $\hat{p}_s^{\bigcirc}$ for all root segments in the mesh over the domain depth for the case $p_{r,c} = -5 \times 10^5$ Pa. For PS, $\hat{p}_s^{\bigcirc}$ is computed as a numerical integral over all coupling surface facets; for CSS

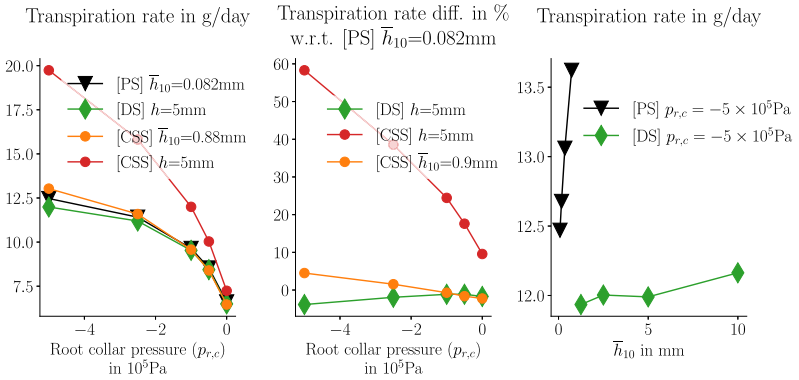

Fig. 14. Predicted transpiration rates for different grids and methods. [DS] distributed source method (this paper), [CSS] cylinder surface method, cf. [3,34], [PS] projection method, resolved root-soil interface, cf. [23]. The symbol $\overline{h}_{10}$ denotes the average diameter of the smallest 10% of the cells. The DS method uses a uniform mesh with cell diameter $h \equiv \overline{h}_{10}$. The coarse mesh for the CSS method is the same uniform mesh as for DS. The fine mesh for CSS is a locally refined mesh.

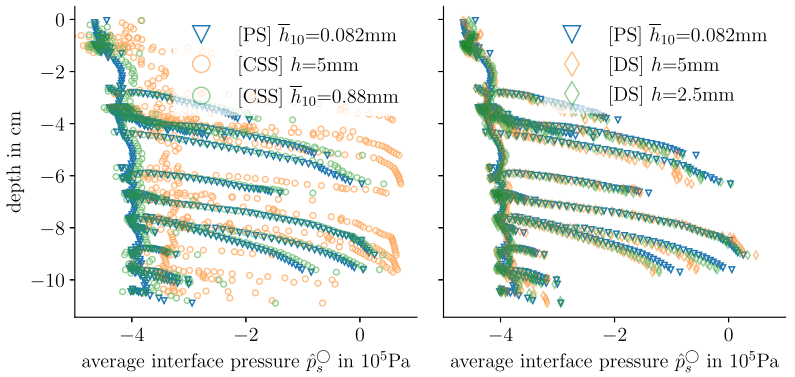

Fig. 15. Average soil pressure on the interface. $\hat{p}_s^{\bigcirc}$ for different methods and $p_{r,c} = -5 \times 10^5$ Pa. [DS] distributed source method (this paper), [CSS] cylinder surface method, cf. [3,34], [PS] projection method, resolved root-soil interface, cf. [23]. The symbol $\overline{h}_{10}$ denotes the average diameter of the smallest 10% of the cells. The DS method uses a uniform mesh with cell diameter $h \equiv \overline{h}_{10}$. The values are computed per root segment. Meshes for CSS are 8k, 1.9M cells, for DS 8k, 61k cells, and for PS 12M cells, respectively.

as numerical integral over the cylinder surface; for DS it is the reconstructed value using the proposed reconstruction algorithm Eq. (3.20). The PS solution is considered a reference, although the results in Fig. 14 suggest that the result is not fully converged, the results can be considered quite accurate with less than 3% difference in the transpiration rate to the DS method and the CSS method with strong local grid refinement. It can be seen that for the CSS method and the coarse grid, the interface soil pressure is overestimated explaining the large overestimation of the transpiration rate. With local grid refinement there is a much closer match with the PS solution. However, we note that in particular for the larger roots (low $\hat{p}_s^{\bigcirc}$), difference between PS and CSS is still clearly visible. On the other hand, the DS closely matches the PS solution even for a coarse grid discretization. The largest difference is observed towards the root tips (highest $\hat{p}_s^{\bigcirc}$). The difference is improved by grid refinement. Note that at $h = 2.5$ mm and given that $\varrho_i = 3R_i$ the kernel support around most smaller root segments is hardly resolved by one mesh cell, cf. Fig. 11. Therefore, this close match between the novel DS method and the PS method using a fully-resolved root-soil interface and more than a thousand times more mesh cells is remarkable. This shows that the root water uptake problem, in particular in drier soils is clearly dominated by large and very localized gradients at the root-soil interface that are difficult to approximate for standard numerical schemes.

Finally, we remark that there is a strong reduction in computational time associated with the advantage of using a coarse grid discretization and a structured cube grid for the three-dimensional domain. While the DS method used 1 s (wall-clock time) per simulation for the 8k grid (5 min for 4M cells), the interface resolving PS method used 2.7 h for 11M cells. The DS method also required on average less Newton iterations. This can be attributed to the fact that the nonlinearity in D_b is shifted into the reconstruction algorithm, whereas the numerical solution is regularized. For the projection method the large interface gradients have to be approximated by the discrete solution.

5. Summary and final remarks

Mixed-dimensional methods are efficient methods for solving coupled mixed-dimensional PDEs arising from flow and transport processes in systems with tubular network systems embedded in a bulk domain. The bulk is represented by a three-dimensional mesh, the tubes are given as a network of cylinder center-line segments, and the meshes are typically non-matching. If the diffusion coefficient in the bulk domain depends on the unknown concentration a coupled nonlinear diffusion equation has to be solved. Its solution may exhibit large local gradients at the tube-bulk interface. This is for example the case when modeling water transport in soils with embedded root systems. Roots take up water from the soil and transport it upwards toward the atmosphere. In particular in dry soils, water uptake causes a strong local drop in the hydraulic conductivity leading to large pressure gradients around root segments.

We introduced an efficient numerical method for the solution of such nonlinear mixed-dimensional PDEs. The method is based on source distribution in a finite neighborhood region of the network, in combination with a nonlinear reconstruction scheme for interface unknowns. The method is based on several approximations we have analyzed. We estimated the errors associated with the approximations and showed in series of numerical verification tests that these errors remain small in practical applications. We used the new method to simulate root water uptake using a realistic root network. In comparison with existing methods, we showed that the novel method outperforms other methods in both accuracy and efficiency. While the numerical results clearly show that the method accurately solves stationary problems, time-dependent problems are yet to be investigated in future work. However, preliminary results with root water uptake and slowly varying conditions (e.g. diurnal cycles) suggest that the method remains accurate.

Due to the possibility to use coarse computational grids in comparison with the tube diameter of the embedded networks, the presented method allows to perform simulations with large networks with reasonable 3D grid resolutions. Coarse grid discretizations ($h \gg R$) in mixed-dimensional methods effectively lead to a distribution of any exchange source term q of an embedded tube into a neighborhood of diameter h. However, since local variations of a bulk unknown u_b cannot be resolved, the approximation of a source term depending on u_b evaluated on the tube-bulk interface suffers from significant errors. By deliberately introducing a distribution kernel for the source term, u_b is locally modified and deviates from the real solution. However, by construction, the behavior of u_b in the vicinity of the tube-bulk interface is better understood and it is possible to develop an interface reconstruction scheme, see Eq. (3.13) and Section 3.2. We have shown that the reconstruction significantly reduces the discretization error. Another approach is the Peaceman well model known in reservoir engineering [30,38,39]. Peaceman devises a reconstruction method eliminating discretization errors for one specific discretization scheme, and with some assumptions on the structure of the mesh and the orientation of the well tube. Methods based on the discrete formulation have also been explored for root water uptake simulations [24,40,14]. In contrast, the distributed source approach used in this work is formulated in the continuous setting which allows the analysis of the problem from a different perspective, and is applicable for any discretization scheme. Furthermore, the model remains valid in the case that the discretization length is smaller than the tube radius, which may readily occur if the tube radii vary significantly in the network (e.g. large root systems). The distribution kernel effectively relaxes the strong discretization length restriction on the tube radius present in methods that require a direct numerical approximation of the interface unknown [18]. Our observations extend the results of [18] to the nonlinear case and indicate that as soon as the discretization length is in the range of the kernel radius ($h \approx \varrho$) the error in the source term is already reasonably small for many application scenarios. In effect, this property allows to improve the solution accuracy for simulations where finer grid discretization is not feasible, e.g. because of high computational costs.

CRediT authorship contribution statement

Timo Koch: Conceptualization, Data curation, Investigation, Methodology, Project administration, Software, Supervision, Validation, Visualization, Writing – original draft. **Hanchuan Wu:** Data curation, Investigation, Software, Validation, Visualization, Writing – review & editing. **Martin Schneider:** Conceptualization, Formal analysis, Methodology, Project administration, Supervision, Writing – original draft.

Declaration of competing interest

The authors declare that they have no known competing financial interests or personal relationships that could have appeared to influence the work reported in this paper.

Acknowledgements

We want to thank Kent-André Mardal and Rainer Helmig for constructive comments on the initial manuscript. This work was financially supported by the German Research Foundation (DFG), within the Collaborative Research Center on Interface-Driven Multi-Field Processes in Porous Media (SFB 1313, Project Number 327154368). We would also like to thank the German Research Foundation for supporting this work by funding – EXC2075 – 390740016 (SimTech) under Germany's Excellence Strategy. T. Koch also acknowledges funding from the European Union's Horizon 2020 research and innovation programme under the Marie Skłodowska-Curie grant agreement No 801133.

Appendix A. Exponential diffusion coefficient function

For numerical verification tests, we choose the following exponential function for $D_b(u_b)$ as an example for a strongly nonlinear function (depending on the rate parameter k),

$$\begin{aligned} D_b(u_b) &= \max(D_0 \exp\{k(u_b-1)\}, D_{\min}) \\ &= \begin{cases} D_{\min} & u_b \le u_c \\ D_0 \exp\{k(u_b-1)\} & u_b > u_c \end{cases}, \end{aligned} \tag{A.1}$$

where D_0 is a constant diffusion coefficient, $u_c = 1 + \frac{1}{k}\ln\{\frac{D_{\min}}{D_0}\}$ such that D_b is continuous, and $D_{\min} = D_0\epsilon$ (where $\epsilon > 0$ is a small constant) is a minimal diffusion coefficient, for the purpose of rendering the Kirchhoff transformation, $T(u_b)$, and its inverse, $T^{-1}(\psi)$, well-defined on all of $\mathbb{R}$ (see Section 3.1).

We obtain analytical expressions for $T(u_b)$ and $T^{-1}(\psi)$ by splitting the integral range depending on the sign of u_c and depending which one of u_b and u_c is larger. The Kirchhoff transformation, as defined in Eq. (3.1), is given for $u_c \le 0$ by

$$T(u_b) = \begin{cases} D_{\min}(u_b - u_c) + \frac{D_0}{k}\left(D_{b,r}(u_c) - D_{b,r}(0)\right) & u_b \le u_c \\ \frac{D_0}{k}\left(D_{b,r}(u_b) - D_{b,r}(0)\right) & u_b > u_c, \end{cases} \tag{A.2}$$

and for $u_c > 0$ by

$$T(u_b) = \begin{cases} D_{\min} u_b & u_b \le u_c \\ \frac{D_0}{k}\left(D_{b,r}(u_b) - D_{b,r}(u_c)\right) + D_0 D_{b,r}(u_c) u_c & u_b > u_c, \end{cases} \tag{A.3}$$

where $D_{b,r}(u_b) = \exp\{k(u_b-1)\}$. The inverse transformation, for the case that $u_c \le 0$, is given by

$$T^{-1}(\psi) = \begin{cases} \frac{1}{D_{\min}}\left(\psi - \frac{D_0}{k}\left(D_{b,r}(u_c) - D_{b,r}(0)\right)\right) + u_c & \psi \le T(u_c) \\ 1 + \frac{1}{k}\ln\left\{\frac{k}{D_0}\psi + D_{b,r}(0)\right\} & \psi > T(u_c), \end{cases} \tag{A.4}$$

and for the case that $u_c > 0$, by

$$T^{-1}(\psi) = \begin{cases} \frac{1}{D_{\min}}\psi & \psi \le T(u_c) \\ 1 + \frac{1}{k}\ln\left\{\frac{k}{D_0}(\psi - D_0 D_{b,r}(u_c)u_c) + D_{b,r}(u_c)\right\} & \psi > T(u_c). \end{cases} \tag{A.5}$$

The functions $D_b(u_b)$, $T(u_b)$, and $T^{-1}(\psi)$ are plotted for $D_0 = 1$ and $\epsilon = 1 \times 10^{-6}$ in Fig. 3.

Appendix B. Error estimate for arbitrarily-oriented tubes in 3D

In the following we want to derive an estimate for $|\Pi_{P_i} f_j - f_j(\boldsymbol{x}_i)|$. Using the multivariate Taylor expansion for f_j for any $\boldsymbol{x} \in B_{R_i}(\boldsymbol{x}_i)$ yields

$$f_j(\boldsymbol{x}) = f_j(\boldsymbol{x}_i) + \nabla f_j(\boldsymbol{x}_i)\cdot(\boldsymbol{x} - \boldsymbol{x}_i) + \mathcal{R}_2(\boldsymbol{x} - \boldsymbol{x}_i), \tag{B.1}$$

with the second-order residual $|\mathcal{R}_2(\boldsymbol{x} - \boldsymbol{x}_i)| \le \frac{C}{2}\|\boldsymbol{x} - \boldsymbol{x}_i\|_2^2$ and the constant

$$C := \sup_{|\alpha|=2}\left(\sup_{\boldsymbol{x}\in B_{R_i}(\boldsymbol{x}_i)} |\partial^\alpha f_j(\boldsymbol{x})|\right). \tag{B.2}$$

Applying the averaging operator to Eq. (B.1) results in

$$|\Pi_{P_i} f_j - f_j(\boldsymbol{x}_i)| \le \frac{C}{2} R_i^2. \tag{B.3}$$

We then assume that the contributions from neighboring tubes contributions from all neighboring tubes j can be formulated in terms of line sources and that the tubes are non-overlapping. The influence of segment sources decays faster with the distance than for the line source, so we consider this a conservative assumption. The corresponding functions f_j are given by

$$f_j(\boldsymbol{x}) = \begin{cases} \frac{1}{2\pi}\left[\frac{||\boldsymbol{x} - \mathcal{E}_j^\perp(\boldsymbol{x})||_2^2}{2\varrho_j^2} + \ln\left(\frac{\varrho_j}{R_j}\right) - \frac{1}{2}\right] & ||\boldsymbol{x} - \mathcal{E}_j^\perp(\boldsymbol{x})||_2 \le \varrho_j, \\ \frac{1}{2\pi}\left[\ln\left(\frac{||\boldsymbol{x} - \mathcal{E}_j^\perp(\boldsymbol{x})||_2}{R_j}\right)\right] & \text{else}, \end{cases} \tag{B.4}$$

where $\mathcal{E}_j^{\perp}$ orthogonally projects $\boldsymbol{x}$ onto the centerline of tube j.

For such functions (assuming non-overlapping kernel support regions), the constant C can explicitly be estimated by calculating the second-order derivatives. We note that gradients of the assumed f_j are aligned with the radial direction of a cylinder coordinate system (r, θ, s) implied by centerline j. Therefore, it is enough to analyze radial derivatives of f_j:

$$\frac{\partial f_j}{\partial r} = \frac{1}{2\pi r}, \quad \frac{\partial^2 f_j}{\partial r^2} = -\frac{1}{2\pi r^2}. \tag{B.5}$$

With the definition of C, this results in the estimate

$$\begin{aligned} |\Pi_{P_i} f_j - f_j(\boldsymbol{x}_i)| &\leq \frac{R_i^2}{4\pi \inf\limits_{\boldsymbol{x} \in B_{R_i}(\boldsymbol{x}_i)} \|\boldsymbol{x} - \mathcal{E}_j^{\perp}(\boldsymbol{x})\|_2^2} \\ &= \frac{R_i^2}{4\pi \left(\|\boldsymbol{x}_i - \mathcal{E}_j^{\perp}(\boldsymbol{x}_i)\|_2 - R_i\right)^2}, \end{aligned} \tag{B.6}$$

where for the last equality we have used the assumption that $\mathcal{E}_j^{\perp}(\boldsymbol{x}_i) \notin B_{R_i}(\boldsymbol{x}_i)$.

References

[1] V.M. Dunbabin, J. a. Postma, A. Schnepf, L. Pagès, M. Javaux, L. Wu, D. Leitner, Y.L. Chen, Z. Rengel, A.J. Diggle, Modelling root-soil interactions using three-dimensional models of root growth, architecture and function, Plant Soil 372 (2013) 93–124, https://doi.org/10.1007/s11104-013-1769-y.

[2] C. D'Angelo, Finite element approximation of elliptic problems with Dirac measure terms in weighted spaces: applications to one- and three-dimensional coupled problems, SIAM J. Numer. Anal. 50 (1) (2012) 194–215, https://doi.org/10.1137/100813853.

[3] T. Köppl, E. Vidotto, B. Wohlmuth, P. Zunino, Mathematical modeling, analysis and numerical approximation of second-order elliptic problems with inclusions, Math. Models Methods Appl. Sci. 28 (05) (2018) 953–978, https://doi.org/10.1142/S0218202518500252.

[4] F. Laurino, P. Zunino, Derivation and analysis of coupled PDEs on manifolds with high dimensionality gap arising from topological model reduction, ESAIM: Math. Model. Numer. Anal. 53 (6) (2019) 2047–2080, https://doi.org/10.1051/m2an/2019042.

[5] C. D'Angelo, Multiscale Modelling of Metabolism and Transport Phenomena in Living Tissues, Bibliotheque de l'EPFL, Lausanne, 2007.

[6] W.R. Gardner, Dynamic aspects of water availability to plants, Soil Sci. 89 (2) (1960) 63–73, https://doi.org/10.1097/00010694-196002000-00001.

[7] C. Doussan, L. Pages, G. Vercambre, Modelling of the hydraulic architecture of root systems: an integrated approach to water absorption—model description, Ann. Bot. 81 (2) (1998) 213–223, https://doi.org/10.1006/anbo.1997.0540.

[8] M. Javaux, T. Schröder, J. Vanderborght, H. Vereecken, Use of a three-dimensional detailed modeling approach for predicting root water uptake, Vadose Zone J. 7 (3) (2008) 1079, https://doi.org/10.2136/vzj2007.0115.

[9] R. Helmig, et al., Multiphase Flow and Transport Processes in the Subsurface: A Contribution to the Modeling of Hydrosystems, Springer-Verlag, 1997, p. 1997.

[10] Y. Mualem, A new model for predicting the hydraulic conductivity of unsaturated porous media, Water Resour. Res. 12 (3) (1976) 513–522, https://doi.org/10.1029/WR012i003p00513.

[11] M.T. Van Genuchten, A closed-form equation for predicting the hydraulic conductivity of unsaturated soils, Soil Sci. Soc. Am. J. 44 (5) (1980) 892–898, https://doi.org/10.2136/sssaj1980.03615995004400050002x.

[12] M.T. Tyree, The cohesion-tension theory of sap ascent: current controversies, J. Exp. Bot. 48 (10) (1997) 1753, https://doi.org/10.1093/jxb/48.10.1753.

[13] E. Steudle, The cohesion-tension mechanism and the acquisition of water by plant roots, Annu. Rev. Plant Physiol. Plant Mol. Biol. 52 (1) (2001) 847–875, https://doi.org/10.1146/annurev.arplant.52.1.847.

[14] T.H. Mai, A. Schnepf, H. Vereecken, J. Vanderborght, Continuum multiscale model of root water and nutrient uptake from soil with explicit consideration of the 3d root architecture and the rhizosphere gradients, Plant Soil 439 (1) (2019) 273–292, https://doi.org/10.1007/s11104-018-3890-4.

[15] C.I. McDermott, A.R. Randriamanjatosoa, H. Tenzer, O. Kolditz, Simulation of heat extraction from crystalline rocks: the influence of coupled processes on differential reservoir cooling, Geothermics 35 (3) (2006) 321–344, https://doi.org/10.1016/j.geothermics.2006.05.002.

[16] M.G. Blöcher, G. Zimmermann, I. Moeck, W. Brandt, A. Hassanzadegan, F. Magri, 3d numerical modeling of hydrothermal processes during the lifetime of a deep geothermal reservoir, Geofluids 10 (3) (2010) 406–421, https://doi.org/10.1111/j.1468-8123.2010.00284.x.

[17] D. Mottaghy, H.-D. Vosteen, R. Schellschmidt, Temperature dependence of the relationship of thermal diffusivity versus thermal conductivity for crystalline rocks, Int. J. Earth Sci. 97 (2) (2007) 435–442, https://doi.org/10.1007/s00531-007-0238-3.

[18] T. Koch, M. Schneider, R. Helmig, P. Jenny, Modeling tissue perfusion in terms of 1d-3d embedded mixed-dimension coupled problems with distributed sources, J. Comput. Phys. 410 (2020) 109370, https://doi.org/10.1016/j.jcp.2020.109370.

[19] K.O. Friedrichs, The identity of weak and strong extensions of differential operators, Trans. Am. Math. Soc. 55 (1) (1944) 132–151, https://doi.org/10.1090/S0002-9947-1944-0009701-0.

[20] K.O. Friedrichs, On the differentiability of the solutions of linear elliptic differential equations, Commun. Pure Appl. Math. 6 (3) (1953) 299–326, https://doi.org/10.1002/cpa.3160060301.

[21] Q.A. Dang, M. Ehrhardt, On Dirac delta sequences and their generating functions, Appl. Math. Lett. 25 (12) (2012) 2385–2390, https://doi.org/10.1016/j.aml.2012.07.009.

[22] D. Cerroni, F. Laurino, P. Zunino, Mathematical analysis, finite element approximation and numerical solvers for the interaction of 3d reservoirs with 1d wells, GEM Int. J. Geomath. 10 (1) (Jan 2019) 4, https://doi.org/10.1007/s13137-019-0115-9.

[23] T. Koch, Projection-based resolved interface mixed-dimension method for embedded tubular network systems, arXiv:2106.06358, 2021.

[24] T. Schröder, M. Javaux, J. Vanderborght, B. Körfgen, H. Vereecken, Effect of local soil hydraulic conductivity drop using a three-dimensional root water uptake model, Vadose Zone J. 7 (3) (2008) 1089–1098, https://doi.org/10.2136/vzj2007.0114.

[25] H.S. Carslaw, J.C. Jaeger, Conduction of Heat in Solids, 2nd edition, Clarendon Press, 1959, p. 1959.

[26] H. Berninger, R. Kornhuber, O. Sander, Fast and robust numerical solution of the Richards equation in homogeneous soil, SIAM J. Numer. Anal. 49 (6) (2011) 2576–2597, https://doi.org/10.1137/100782887.

[27] T. Koch, D. Gläser, K. Weishaupt, S. Ackermann, M. Beck, B. Becker, S. Burbulla, H. Class, E. Coltman, S. Emmert, T. Fetzer, C. Grüninger, K. Heck, J. Hommel, T. Kurz, M. Lipp, F. Mohammadi, S. Scherrer, M. Schneider, G. Seitz, L. Stadler, M. Utz, F. Weinhardt, B. Flemisch, Dumu^{x} 3 – an open-source simulator for solving flow and transport problems in porous media with a focus on model coupling, Comput. Math. Appl. (2020), https://doi.org/10.1016/j.camwa.2020.02.012.

[28] O. Sander, T. Koch, N. Schröder, B. Flemisch, The dune foamgrid implementation for surface and network grids, Arch. Numer. Softw. 5 (1) (2017) 217–244, https://doi.org/10.11588/ans.2017.1.28490.
[29] M. Mori, M. Sugihara, The double-exponential transformation in numerical analysis, J. Comput. Appl. Math. 127 (1) (2001) 287–296, https://doi.org/10.1016/S0377-0427(00)00501-X.
[30] D.W. Peaceman, Interpretation of well-block pressures in numerical reservoir simulation, Soc. Pet. Eng. J. 18 (03) (1978) 183–194.
[31] R. Hsu, T.W. Secomb, A Green's function method for analysis of oxygen delivery to tissue by microvascular networks, Math. Biosci. 96 (1) (1989) 61–78, https://doi.org/10.1016/0025-5564(89)90083-7.
[32] L. Cattaneo, P. Zunino, Computational models for fluid exchange between microcirculation and tissue interstitium, Netw. Heterog. Media 9 (1) (2014), https://doi.org/10.3934/nhm.2014.9.135.
[33] Ingeborg G. Gjerde, Kundan Kumar, Jan M. Nordbotten, Barbara Wohlmuth, Splitting method for elliptic equations with line sources, ESAIM: M2AN 53 (5) (2019) 1715–1739, https://doi.org/10.1051/m2an/2019027.
[34] T. Koch, K. Heck, N. Schröder, H. Class, R. Helmig, A new simulation framework for soil-root interaction, evaporation, root growth, and solute transport, Vadose Zone J. 17 (2018) 1, https://doi.org/10.2136/vzj2017.12.0210.
[35] A. Schnepf, C.K. Black, V. Couvreur, B.M. Delory, C. Doussan, A. Koch, T. Koch, M. Javaux, M. Landl, D. Leitner, G. Lobet, T.H. Mai, F. Meunier, L. Petrich, J.A. Postma, E. Priesack, V. Schmidt, J. Vanderborght, H. Vereecken, M. Weber, Call for participation: collaborative benchmarking of functional-structural root architecture models. The case of root water uptake, Front. Plant Sci. 11 (2020) 316, https://doi.org/10.3389/fpls.2020.00316.
[36] T. Koch, Benchmark C1.2 data set - numerical results reference solution, DaRUS, 2019, https://doi.org/10.18419/darus-471.
[37] T. Koch, Mixed-dimension models for flow and transport processes in porous media with embedded tubular network systems, Ph.D. thesis, University of Stuttgart, 2020, https://doi.org/10.18419/opus-10975.
[38] D.W. Peaceman, Interpretation of well-block pressures in numerical reservoir simulation with nonsquare grid blocks and anisotropic permeability, Soc. Pet. Eng. J. 23 (03) (1983) 531–543, https://doi.org/10.2118/10528-PA.
[39] T. Koch, R. Helmig, M. Schneider, A new and consistent well model for one-phase flow in anisotropic porous media using a distributed source model, J. Comput. Phys. 410 (2020) 109369, https://doi.org/10.1016/j.jcp.2020.109369.
[40] N. Beudez, C. Doussan, G. Lefeuve-Mesgouez, A. Mesgouez, Influence of three root spatial arrangement on soil water flow and uptake. Results from an explicit and an equivalent, upscaled, model, Proc. Environ. Sci. 19 (2013) 37–46, https://doi.org/10.1016/j.proenv.2013.06.005, four Decades of Progress in Monitoring and Modeling of Processes in the Soil-Plant-Atmosphere System: Applications and Challenges (2013).